THESIS FOR THE DEGREE OF LICENTIATE OF ENGINEERING

Combining Nanoplasmonics and Nanofluidics for Single Particle Catalysis

DAVID ALBINSSON

CHALMERS

Department of Physics
CHALMERS UNIVERSITY OF TECHNOLOGY
Gothenburg, Sweden 2018

Combining Nanoplasmonics and Nanofluidics for Single Particle Catalysis

DAVID ALBINSSON

Department of Physics

Chalmers University of Technology

SE-412 96 Gothenburg

Sweden

Telephone + 46 (0)31-772 1000

Cover:

Artistic rendering of a nanochannel containing plasmonic nanoparticles that are probed using light during a catalytic reaction.

Printed at Chalmers Reproservice

Gothenburg, Sweden 2018

Combining Nanoplasmonics and Nanofluidics for Single Particle Catalysis

David Albinsson
Department of Physics
Chalmers University of Technology

Abstract

Nanoparticles are, due to their large exposed surface area, widely used in the field of heterogeneous catalysis where they accelerate and steer chemical reactions. Although catalysis has been known about for centuries, the scrutiny of catalysts under realistic application conditions is still a major challenge. This difficulty originates from the fact that real catalyst materials are very complex, often consisting of large ensembles of nanoparticles that all are unique. Furthermore, the typically used macroscopic reactors in catalysis studies gives rise to locally, at the level of the active site, ill-defined reactant concentrations and diffusion limitations.

To overcome these limitations, on one hand, techniques are being developed that are sensitive enough to probe individual catalytic particles and that at the same time can operate under realistic reaction conditions. On the other hand, strategies to more carefully control the amount and structure of catalyst material, as well as to precisely control mass transport to and from the active catalyst, are being investigated by scaling down the size of the used chemical reactor. To further push the limit of downsizing, in this thesis, I present a miniaturized reactor platform based on nanofluidic channels that have been carefully decorated with catalytic nanoparticles, and that is integrated with plasmonic nanospectroscopy readout. This optical technique relies on the nanoscale phenomenon known as the Localized Surface Plasmon Resonance (LSPR) and enables the study of individual metal nanoparticles *in operando* by means of dark-field scattering spectroscopy.

As the first step in this development, we constructed a nanofluidic device with integrated plasmonic nanoparticles to detect minute changes in the liquid flowing through the channels, as well as molecules binding to the nanoparticles. As the second step, we developed the nanofluidic system with an integrated heater and to facilitate gas flow through the nanochannels with the possibility to connect to a mass spectrometer for on-line product analysis. This system was then successfully used to correlate activity with surface and bulk oxidation state changes taking place on individual catalytic Cu and Pt nanoparticles during CO oxidation, measured by means of plasmonic nanospectroscopy. To this end, in a separate study, I also employed the plasmonic approach to study the oxidation process of Cu nanoparticles both experimentally and by electrodynamics simulations.

Keywords: LSPR, plasmonic sensing, heterogeneous catalysis, single particle catalysis, Cu oxidation, CO oxidation, nanocatalyst, dark field scattering spectroscopy, nanofluidics, nanoreactor

List of appended papers

This thesis is based on the work presented in the following papers:

Paper I

Single Particle Nanoplasmonic Sensing in Individual Nanofluidic Channels.
Joachim Fritzsche, David Albinsson, Michael Fritzsche, Tomasz J. Antosiewicz, Fredrik Westerlund, Christoph Langhammer
Nano Letters, **16,** 7857–7864 (2016).

Paper II

Plasmonic Heterodimers for Drift-Free Sensing of Cu Nanoparticle Oxidation and the Nanoscale Kirkendall Effect
David Albinsson, Sara Nilsson, Tomasz J. Antosiewicz, and Christoph Langhammer
In Manuscript

Paper III

Nanofluidic Reactors for Single Particle Catalysis
David Albinsson, Stephan Bartling, Sara Nilsson, Henrik Ström, Joachim Fritzsche and Christoph Langhammer
In Manuscript

My contribution to appended papers

Paper I

I performed the FDTD simulations and thiol binding experiments as well as wrote a part of the manuscript.

Paper II

I fabricated the samples, performed all the experiments, except the TEM measurements, performed the FDTD simulations, analyzed the data and wrote the first draft of the manuscript.

Paper III

I fabricated the samples, took part in constructing the experimental system connecting the nanoreactor to the macroscopic world, performed the experiments and the FDTD simulations, analyzed the data and wrote the first draft of the manuscript.

Table of Contents

1 Introduction

During the past decades, progress in the field of nanotechnology has resulted in the ability to characterize and manipulate matter on length scales as small as single atoms.[1] This development is driven by the fact that materials that are scaled down in size to the nanometer regime (10^{-9} m), which is on the order of 100 000 times smaller than the diameter of a human hair, can have significantly different properties than at the macroscopic scale. Understanding why and learning how to control these new properties has proven to have a large impact on many fields of modern technology, including electronics[2], medicine[3] and catalysis.[4]

Although used for centuries to, e.g., stain glass,[5] the ability to study and understand nanomaterials and nanoparticles is rather recent and the consequence of the invention of techniques that enable imaging and characterization of structures down to the level of single atoms.[1] In addition, state-of-the-art nanotechnology enables the tailoring of nanostructures with exceptional precision in terms of size, shape and composition[1,6] and thus opens up the possibility to design task-specific materials at the atomic level.

One field that has benefitted greatly from the progress in nanotechnology is heterogeneous catalysis where nanostructures and particles are used to enable and control chemical reactions.[4] The word "catalyst" is something that the layman probably has heard about in the context of cars, where it refers to the part or the exhaust system that removes pollutants from the exhaust gas stream. Furthermore, applications of catalysis are approximated to be involved in up to 90% of the products made by the chemical industry,[7] they play an essential role in assisting biological reactions (often in the form of enzymes) and are the key to numerous renewable energy technologies, such as fuel cells. The reason why catalysts are so widely used is that they have the ability to make otherwise very (or even infinitely) slow chemical reactions proceed much faster by lowering energy barriers that the reactants have to overcome to form a certain product. Therefore the use of catalysts is beneficial both from an environmental and an economical point of view. Catalysts used in a man-made system typically consist of solid nanostructures that are used to catalyze reactions of liquid or gas phase reactants. This is known as heterogeneous catalysis. The active phase often consists of noble metals such as Palladium (Pd), Platinum (Pt) or Rhodium (Rh), which are all quite scarce and therefore expensive. To maximize the active surface area per gram of used catalyst these materials are typically scaled down to nanoparticles (1-100 nm), which are then dispersed onto a highly porous support materials such as Alumina (Al_2O_3), Silica (SiO_2) or Titania (TiO_2).

Developing efficient catalysts is a multi-disciplinary task that requires cooperation from science and engineering, much due to the many length scales that are spanned by a catalyst.[8] Starting from the Ångström level at which the bonds in molecules are broken and formed, and spanning from the active nanoparticles (10^{-9} – 10^{-7} m) to the support materials (10^{-6} m) and all the way up to industrially sized catalyst beds (>1 m). Although heavily researched, there are still many open questions related to what exactly is controlling a catalytic process at application conditions. More specifically, to get the true picture of a catalytic process, one has to be able to characterize both the active catalyst

materials and the chemical transformations on them with very high spatial, as well as temporal resolution, and at demanding conditions in terms of temperature and pressure. At the same time, the transport of reactants to and from the catalyst particle surface has to be studied since it is strongly affected by the dimensions of the surrounding environment (e.g. a nano- or mesopore[9]), as well as by other catalytic particles in the vicinity.[7]

To this end, today, there exist many techniques, e.g. electron microscopy, X-ray photoelectron spectroscopy (XPS) and scanning tunneling microscopy (STM),[7] to characterize so-called model catalysts (typically single crystalline surfaces) under ideal conditions (pressures below 10^{-5} mbar). For example, such model studies have generated invaluable insights into the fundamental steps involved in a catalytic process, with a famous example being the ability to track surface coverage of different species changing in time and space on a catalyst surface.[8] However, the experimental probes used are often limited to low pressure or even (ultra high) vacuum conditions. To this end, it is well-known that reactions do not proceed in the same way at ambient pressure conditions.[10] In addition, the typically used single crystal model catalyst materials are a simplification of a commercial catalyst material comprised of a chemically complex support and nanoparticles. This creates a mismatch between the conditions, as well as the materials, used in catalysis research and technical catalysts used in industry, which is commonly referred to as the *pressure* and *materials gap*. Hence, to bridge the *pressure gap*, it is necessary to develop new experimental means that allow the study of catalytic reactions and the active catalyst nanomaterials under realistic application conditions, also known as *in-operando* or *in-situ* techniques.[10–14] To bridge the *materials gap* it is required to replace the model surfaces used for research with real catalyst materials such as nanoparticles. The latter step, however, then brings along yet another experimental challenge due to the fact that it, at the atomic scale, is extremely difficult to create an ensemble of perfectly identical nanoparticles. In other words, to see beyond the averaged response of many slightly different nanoparticles, it is necessary to study individual nanoparticles, which is a grand experimental challenge that requires very sensitive instruments and tailored experimental designs.[15]

1.1 Scope of this thesis

This thesis has been focused on the development of an experimental concept that enables the *operando* characterization of individual catalytic nanoparticles. This was done by means of optical spectroscopy based on plasmonic sensing, combined with analysis of the formed reaction products by means of a nanofluidic reactor platform connected to a mass spectrometer.

Nanofluidics is, as the name suggests, the field related to studying and controlling fluids on length scales < 100 nm.[16,17] The field has emerged in the footsteps of microfluidics as a consequence of the continuously growing ability to fabricate smaller structures with high precision. Because the physical length scales achieved in nanofluidics can be smaller than the characteristic scaling lengths of fluids, fascinating new phenomena can emerge. For example, when the spatial dimensions of a system approaches the distance between consecutive molecular collisions (mean free path) the flow can no longer be described by conventional continuum fluid dynamics.[18] Additionally, by confining molecules using

nanofluidic channels they can be guided to very precise regions, e.g. directly to selected nanoparticles, and thus induce specific interactions.

Plasmonic sensing is based on the localized surface plasmon resonance (LSPR) phenomenon, that results in vivid coloration of metallic particles when they are scaled down to a size smaller than the wavelength of visible light (<400 nm). This stems from a collective oscillation of the free electrons in the metal, which can be resonantly excited by visible light. Because these resonances are very sensitive to changes that occur in/on the plasmonic nanoparticles, as well as in their close nano-surroundings, they can be used as highly sensitive probes for the detection of molecules, chemical processes and catalytic reactions that occur at the nanoscale at *operando* conditions.[19–25] To pave the way for the use of plasmonic probes to study nanoparticles at the single particle level during a catalytic reaction, I performed a study of the oxidation of Cu nanoparticles by means of plasmonic sensing.

The main part of this thesis was to develop the principle and necessary nanofabrication to combine single particle plasmonic nanoprobes with nanofluidic structures to allow for nanoscale sensing *inside* extremely confined volumes in the single particle catalysis context. As the first step in this quest, a more "traditional" liquid phase nanofluidic system was integrated with plasmonic nanoparticles that are individually optically addressable by means of dark-field scattering spectroscopy. For a first proof-of-principle, the developed nanofluidic device was then used to measure minute changes in the fluids flushed through the nanofluidic system via the integrated plasmonic sensing readout, as well as to detect molecular binding events taking place on individual plasmonic Au nanoparticles.

In the second step, we developed an entirely new experimental setup that enabled - for the first time - the operation of a nanofluidic system with a fluid in the gas phase while being connected to a quadrupole mass spectrometer. In this way, it becomes possible to utilize such nanofluidic systems, which we decorate with optically addressable catalyst nanoparticles, as nanoscale chemical flow reactors or *nanoreactors*. As I show by two application examples, these devices enable the direct correlation of the catalyst surface and oxidation state measured *in operando* at the single nanoparticle level with its activity. Secondly it was used to shed light on mass transport limitations occurring at the single particle level in a highly confined volume that mimics the situation in a nanopore of a catalyst support material. Our findings highlight the fact that the conditions inside a chemical reactor can vary significantly in both space and time, and that mass transport at the nanoscale may widely dictate catalyst activity.

2 Optical properties of plasmonic nanoparticles

When metals are reduced to a size smaller than the wavelength of light their optical properties change dramatically, giving rise to vivid coloration of otherwise typically gray shiny materials. These colors stem from a phenomenon caused by resonant collective oscillations of the conduction electrons in the material and are known as Localized Surface Plasmon Resonances (LSPR). Interestingly, these resonances are strongly dependent on a wide set of properties of the nanoparticles, such as the material, size, shape and permittivity surrounding the particle. This chapter will focus on explaining the physics governing the optical properties of metallic nanoparticles, as well as explain why they are interesting.

2.1 Optical properties of bulk metals

Optical properties of all materials are governed by how the materials interact with visible light, that is, the part of the electromagnetic spectrum with a wavelength between 400 to 800 nm. Bulk metals and their shiny appearance is something well known to most of us, and the fact that some metals appear gray, whereas others appear colored, is also common knowledge.

In atoms or molecules, the energy levels that electrons can occupy are discrete and to excite an electron from one energy level to another costs a finite amount of energy. The molecule, via an electronic transition, can thus absorb photons with energy that matches one of the gaps between energy levels. In a semiconductor, a similar absorption process can take place by exciting an electron from the valence band to the conduction band above the band gap. If this absorption occurs in the range of visible light, the material will appear to have color. In contrast, metals have no minimum energy needed to excite an electron to a non-bound state (i.e. no band gap). Instead, when exposed to an electric field such as light, the free electrons in a metal will immediately rearrange to screen the field. As long as they have enough time to be able to fully rearrange and screen the incoming field, the metal will reflect the incident field and thus reflect the light. However, above a certain frequency the electrons will not be able to respond fast enough to the external field. This essentially makes the screening impossible and the electromagnetic wave will not be reflected. This frequency is known as the plasma frequency. Additionally, if the band structure of a certain metal allows for electrons to be excited from a region with high density of states (typically a d-band) to the Fermi level, certain wavelengths of the electromagnetic spectrum can be absorbed by the metal in a fashion similar to the case of semiconductors in what is known as an interband transition. This process is what gives rise to the coloration of, for example, bulk gold, which has an interband transition threshold at 2.5 eV (496 nm) that results in blue light being absorbed, making the appear metal yellow. If the onset for interband transitions has a lower energy than visible light, photons of all colors will be partially absorbed into the metal, making it appear duller and less shiny, which can be seen for, for example, Pd. Physically, the interaction of a metal

(as well as semiconductors and insulators) with incident electromagnetic fields can be described by their complex dielectric function.

2.2 Optical properties of metallic nanoparticles

The fact that metals change their optical properties when scaled down in size is something that has been used for centuries, long before any attempts to understand the physics of why these optical changes occurred had been reported. A classic example of this is the Lycurgus Cup, shown in Figure 2.1, dating back to the 4th century A.D. It has the fascinating optical property that it is perceived to have different colors depending on if its viewed against a dark or a bright background.

Figure 2.1 **The Lycurgus cup.** A Roman-era cup made so that it appears red when light is transmitted through it (left) and green when light is reflected (right). The reason for this optical phenomenon is the metallic nanoparticles in the glass that both scatter and absorb light in the visible range. Images from the website of the British Museum. [26]

The reason is that the glass in the cup contains colloidal metallic nanoparticles (Au, Ag and Cu) that both absorb and scatter light mostly in the green part of the optical spectrum.[5] As a result, the cup appears green when the scattered light is seen and red when transmitted light is seen. The phenomenon giving rise to these colors is known as localized surface plasmon resonance (LSPR) which occurs in structures with free electrons when they are scaled down to a size smaller than the wavelength of light.

Figure 2.2A illustrates a nanoparticle that is smaller than the wavelength of an incident time-dependent electric field. As a consequence of the field, the electrons in the particle are displaced with respect to the atomic cores, resulting in charge separation. In turn, this will give rise to a restoring force that tries to pull the electrons back in place, making the system behave as a damped harmonic oscillator with spring constant and damping depending on the shape, size and material of the particle. Thus, incoming electromagnetic radiation that matches the resonance frequency of the nanoparticle will result in strong absorption and scattering, which in turn gives rise to color if the resonance is in the visible range of the spectrum.

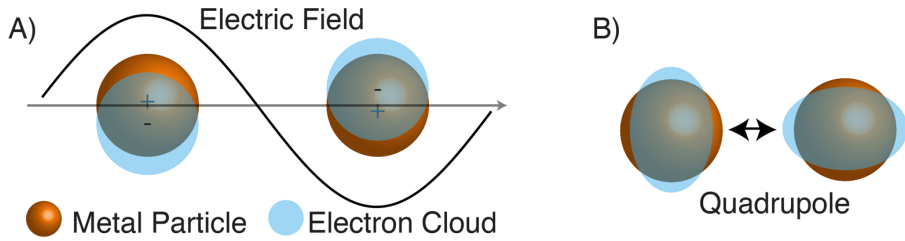

Figure 2.2 – **The localized surface plasmon resonance (LSPR).** A) Schematic illustration of free electrons in a nanoparticle being displaced by an incident time-dependent electric field causing an oscillation of the free electrons. B) Higher order quadrupole resonance.

Due to the displacement of the electrons during a LSPR excitation, a dipolar field is induced close to the particle. For very small particles, this dipolar mode shown in Figure 2.2A dominates, but higher order modes, such as quadrupoles illustrated in Figure 2.2B are also possible, especially as the nanoparticle size is increased.[27] The enhanced field region created by such dipolar or higher order resonances can act as a probe of the dielectric environment surrounding the particle, making it useful as an optical nanoscale sensor in many applications including biosensing, chemical sensing, and gas sensing.[19,21,28–31] For the same reason, it is also the main method that I have used to study minute changes on (single) catalyst nanoparticles in this thesis.

To qualitatively describe the LSPR phenomenon, it is initially sufficient to consider a simplified system consisting of a metallic sphere with a radius much smaller than the wavelength of light. This makes it possible to employ analytical solutions developed by Gustav Mie to calculate the electromagnetic response of the system.[32] For a small spherical particle one can assume that the electrostatic approximation holds, meaning that at a given time, there is no spatial variation of the electric field along the whole sphere. Hence, upon exposure to an electric field, $\boldsymbol{E_0}$, a dipole moment will be induced as:

$$\boldsymbol{P} = \varepsilon_d \alpha \boldsymbol{E_0}$$

Where ε_d is the dielectric function of the embedding medium and α is the polarizability of the sphere that can be expressed as[33]:

$$\alpha(\omega) = 4\pi r^3 \frac{\varepsilon_m - \varepsilon_d}{\varepsilon_m + 2\varepsilon_d} \tag{2.1}$$

where r is the radius of the sphere and ε_m is the frequency dependent dielectric function of the metal. The strength of the particle-light interaction can be expressed as cross-section, and for a perfect sphere an interaction cross-section can be calculated for scattering, absorption and extinction, respectively[33]:

$$C_{absorption} = kIm(\alpha) = 4\pi k r^3 Im\left(\frac{\varepsilon_m - \varepsilon_d}{\varepsilon_m + 2\varepsilon_d}\right) \tag{2.2}$$

$$C_{scattering} = \frac{k^4}{6\pi} abs(\alpha)^2 = \frac{8\pi}{3} k^4 r^6 \left|\frac{\varepsilon_m - \varepsilon_d}{\varepsilon_m + 2\varepsilon_d}\right|^2 \tag{2.3}$$

$$C_{extinction} = C_{absorption} + C_{scattering} \tag{2.4}$$

where $k = \frac{2\pi}{\lambda}$ is the wavenumber of incident light. From these equations we can note that both scattering and absorption are maximized by maximizing the polarizability. Furthermore, we see that scattering scales as r^6, while absorption scales as r^3. This means that larger particles will predominantly scatter light, while smaller ones mainly absorb. For both processes the cross-section will diverge when the denominator goes to zero, i.e. when

$$\varepsilon_m(\omega) = -2\varepsilon_d \tag{2.5}$$

which is the resonance condition for a LSPR.

As briefly mentioned previously, the optical properties of different metals can be quite different, meaning that ε_m varies from metal to metal. However, in a simple picture a metal can be described by the Drude model, which assumes that all conduction electrons are delocalized and free to move, thus ignoring any potential interband transitions. This approximation allows us to describe the complex dielectric function of the metal as:[33]

$$\varepsilon_m(\omega) = 1 - \frac{\omega_p^2}{\omega^2 + i\Gamma\omega} \tag{2.6}$$

where ω_p is the plasma frequency and Γ is a damping parameter that originates from processes taking place in the material to dissipate energy. By further assuming that damping is negligible, putting eq. 2.6 into eq. 2.5 and solving for ω, the LSPR frequency reads as:

$$\omega_{LSPR} = \frac{\omega_P}{\sqrt{1 + 2\varepsilon_d}} \tag{2.4}$$

or expressed in terms of wavelength:

$$\lambda_{LSPR} = \lambda_P\sqrt{2\varepsilon_d + 1} \tag{2.5}$$

where $\lambda_P$is the plasma wavelength defined as $\lambda_P = c/\omega_P$, where c is the speed of light. Although very simplified, this model captures the key aspects of the LSPR, such as its dependence on the surrounding medium, which gives rise to a spectral redshift when its refractive index ($n = \varepsilon_d^2$) is increased. Above we assumed the damping was negligible, however, in real nanoparticles, damping will always be present and it will strongly affect the optical properties of the nanoparticle. The main sources of damping are either radiative processes (scattering), or non-radiative processes, mainly dominated by electron-hole excitations in the metal through intra- and interband transitions. Increasing the damping factor will lower the lifetime of the LSPR and as a result the resonance peak will widen in the frequency domain.

Although the description presented above is very useful for conceptual understanding, real nanostructures neither are ideal spheres nor are their dielectric functions as simple as the form suggested by Drude. To address real materials with realistic shapes in different constellations, other approaches have to be used and will be addressed in the following section.

2.2.1 Effects of material, shape and size

The two most widely used materials in the field of plasmonics are Au and Ag due to their superior optical properties that give rise to narrow LSPR bands in the visible range, as well as due to their chemical inertness (especially in the case of Au). However, the field of plasmonics is not limited to these materials and has been expanded to include Cu, Pt, Pd, Ni, Al,[34–37] alloys of noble metals[38,39] as well as non-metallic materials such as nitrides.[40] Naturally, each of these materials has its own electronic structure that gives rise to different dielectric functions thus different plasmonic properties.

Also size can strongly affect the optical properties of nanoparticles. When the particle size is increased, the incoming field will no longer be the same across the whole particle, which leads to retardation effects. This will result in a phase shift between the incident and induced dipolar field in the particle, which in turn will red shift the resonance. As shown in eq. 2.3, scattering increases rapidly with volume, giving rise to strong radiative damping. Therefore, larger particles are also expected to exhibit more radiative damping, a shorter lifetime and thus a wider resonance peak.[41] The non-radiative damping channel is dominated by absorption and results in a broadening of the resonance peak in materials that have strong absorption in the same range as the LSPR. This is typically seen in materials with allowed interband transitions in the visible range, such as the noble metals like Pt or Pd that have an very broad resonance peak.

To address more complex shapes, analytical solutions that extend Mie's theory for spheres exist for arbitrary spheroids.[27] However, real nanostructures always have more complex shapes and are often placed on substrates that themselves can have complicated surface structure. To simulate the optical properties of such structures one has to rely on numerical solutions to Maxwell's equations.[42] Some examples of methods to do so are Finite difference time domain (FDTD),[43] discrete dipole approximation (DDA),[27] finite element method (FEM), boundary element method (BEM)[44] and the modified long wavelength approximation (MLWA).[27,42] These methods make it possible to predict how individual, or groups of, nanoparticle(s) will respond to an electromagnetic field. Today, one of the most popular methods is FDTD that also has been the tool used in this work to simulate the optical response of nanoparticles and nanofluidic structures.

LSPR hybridization

When two (or more) plasmonic nanostructures are placed in close vicinity, the individual resonators couple and modify the resonance condition of the system.[45–47] The interaction between the resonators can be explained by describing the newly formed system as a coupled harmonic oscillator with its own hybrid resonances that closely resemble the hybridization taking place when molecular bonds are formed.[47,48] Similar to the case of molecular bonds were two orbitals are hybridized to form two new molecular orbitals, one with lower (binding) and one with higher (anti-bonding) energies, the hybridization between two LSPRs results in the formation of two new resonance frequencies with lower and higher energies. In the case of a simple homo-dimer system consisting of two identical spherical particles excited by an EM field polarized along the dimer axis, the hybridization scheme is summarized in Figure 2.3. It shows the original energy levels for the dipolar resonances of the two resonators and the two hybridized states with their corresponding dipoles. From Figure 2.3 one can see that the case where the two dipoles

are oriented in the same direction corresponds to the low energy mode, and the one where they are pointing in the opposite direction is the high energy resonance. Since this higher order resonance has no net dipole moment, it cannot interact with the incoming field of light and is thus not excited, resulting in it being a so-called "dark" mode. If the incident field is instead polarized perpendicular to the dimer axis, the hybridization will be different and therefore dimer structures have a strongly polarization dependent optical response.

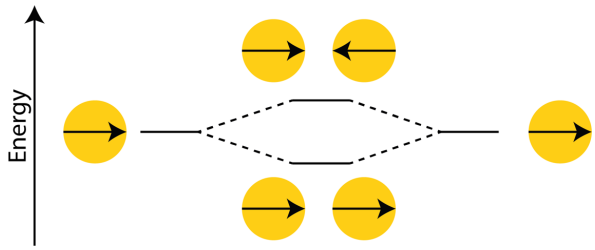

Figure 2.3. **Plasmon hybridization.** As two plasmonic resonators are placed in close vicinity, their modes can couple to form hybridized modes.

More complex structures consisting of differently sized particles of different materials can also be understood by the same hybridization scheme with some added complexity.[46,49] In the case of differently sized structures consisting of the same material, the dark mode is no longer totally dark since the two differently sized particle dipoles will not cancel out completely. Additionally, material dependent effects can give rise to new coupling possibilities between free electron resonances and e.g. interband transitions.[46]

In paper II, heterodimer structures consisting of a Au disk placed next to a smaller Cu nanoparticle formed a hybrid resonance. Presented in Figure 2.4 is an example of the polarization dependent extinction spectra of these nanostructures. Light polarized along the dimer axis is clearly red-shifted compared to the orange line, which represents the spectrum for light polarized perpendicular to the dimer axis.

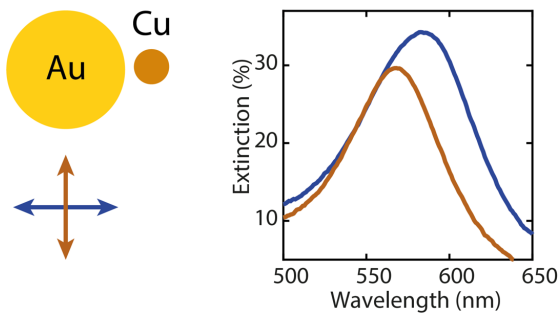

Figure 2.4 **Polarization dependent extinction spectra of a heterodimer.** An Au-Cu heterodimer structure (left) shows a polarization dependent extinction spectrum due to plasmon hybridization, which results in a lower energy resonance for light polarized along the dimer axis compared to light polarized perpendicular to it.

2.3 Plasmonic sensing

As already mentioned, the plasmonic properties of a metal nanoparticle depend on the dielectric properties of the LSPR active material,[50] the size[51] and the particle's surroundings.[52] A change in one of those properties is expected to induce a change in the optical spectrum. Consequently, by measuring absorption and/or scattering spectra from LSPR active structures, small changes in or around the particle can be detected. This is the basis of what is known as plasmonic sensing that was first demonstrated two decades ago[53] when plasmonic Au particles were used as transducers for detecting antigens binding to ligands attached to the particles. A typical optical change of a plasmonic nanoparticle, measured for instance by extinction spectroscopy, is illustrated in Figure 2.5. Here a change in the particles surrounding modifies the resonance condition of the LSPR (eq. 2.5). To quantify the readout the peak is characterized by some well-chosen parameters such as the resonance wavelength (λ_{peak}), the peak intensity (Ext) and the full-width-at-half-maximum (FWHM) of the peak. By tracking how these parameters change over time one can get information about both transient and steady state properties of the system.[54,55]

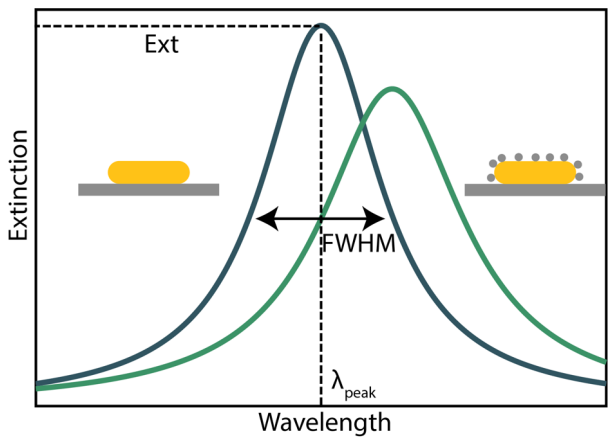

Figure 2.5 **Readout of a plasmonic sensor.** Changes in the plasmonic particle environment or of the particle itself result in a change of the LSPR condition, which is reflected as a change of the far-field extinction (or scattering) spectrum. Typically, the peak descriptors peak position (λ_{peak}), width of the peak (FWHM) and peak extinction (Ext) are used as readout to track changes.

The use of plasmonic structures as sensors today spans a wide set of fields. It is dominated by biological sensors[21,56,57] but has also been used for chemical and gas sensing,[25,58,59] as well as sensing related to catalytic reactions.[19,28,29] Plasmonic sensing has shown to be especially attractive for sensing of solid-state chemical reactions due to the possibility to use it under ambient pressure and at elevated temperatures. Additionally, the measurements can be done in a non-invasive way because only low power visible light is used. Some prominent examples of this is the use of plasmonic nanoparticles to sense the phase transition when Pd and Mg is transformed from a metal to hydride upon absorption of hydrogen.[23,25,31,59–64] Another process that has been studied is Cu oxidation.[65,66] One of

the advantages of using LSPR for sensing is that it is only sensitive to changes in a very small volume surrounding the nanoparticle due to the rapid decay of the induced field away from the surface. Specifically, this sensing decay length is on the order of a few tens of nm at visible frequencies.[57] Furthermore, the field enhancement region around a nanoparticle is determined by how the resonance of the particle is aligned with the polarization of the incoming electric field, as well as by the particle shape (Figure 2.6). Optimizing the latter enables tailoring of the sensitivity such that even single molecules can be detected.[67 20]

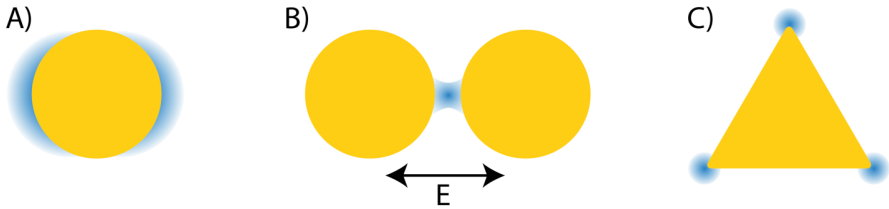

Figure 2.6. **Plasmonic field enhancement.** Schematic depiction of enhanced electric fields around differently shaped plasmonic nanoparticles. A) Around a spherical structure the field enhancement aligns with the incident polarization of the field. B) Dimer structures form hybrid resonances which result in so-called hot spots with highly enhanced field intensities forming between the structures. C) Sharp corners can also result in greatly enhanced field intensities.

2.3.1 Indirect plasmonic sensing

To expand the applicability of plasmonic sensing to a wider range of materials the concept of indirect nanoplasmonic sensing (INPS) can be utilized.[68] The main differentiator that distinguishes INPS from "direct" plasmonic sensing is that the optically active component, the plasmonic nanoantenna, is separated from the material to be "sensed" by a thin spacer layer (Figure 2.7). This makes it possible to study otherwise non-plasmonic or "bad" plasmonic materials by placing them in close vicinity to a good sensing unit. To date, this approach has been used to study properties of Pd nanoparticles undergoing hydride formation both for ensembles[59] and at a single nanoparticle level,[23–25] sintering of catalytic particles[69] and catalytic reactions[22] to name a few. In this thesis, I have used INPS in paper II to study oxidation of small Cu nanoparticles by using a combined Au and Cu heterodimer, and in paper III to study changes in individual Pt nanoparticles during the CO oxidation reaction, by using the Au-SiO_2-Pt arrangement depicted in Figure 2.7.

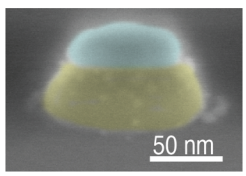

Figure 2.7. **Indirect plasmonic sensor.** Artificially colored SEM micrograph of an indirect nanoplasmonic sensing structure used in this thesis. It is comprised of a Au disk (yellow) used as the sensor to detect changes taking place in the smaller Pt nanoparticle (blue) placed on top. The two particles are separated by a 7 nm SiO_2 spacer layer (not visible).

2.4 Single nanoparticle plasmonic sensing

Today there are several different methods to study LSPRs in individual nanoparticles, each with their own benefits and drawbacks. Here I will try to briefly summarize the main methods and how they work. For a more complete overview I recommend the review article in reference [70].

Single particle methods can be separated into two subgroups: near-field and far-field. Near-field methods rely on studying the particle in the electromagnetic near-field, meaning that the probing is done on the order of a few to a few hundred nm away from the particle itself, while far-field methods probe the particle from a much larger distance. The methods to study near-field properties of plasmonic nanoparticles include: (i) scanning near field optical microscopy, where a mechanical near field probe (typically an AFM-tip) is inserted in close vicinity to a nanoparticle and excites a plasmon through near field interaction;[71–73] (ii) photoelectron emission spectroscopy (PEEM) that studies electrons that are emitted due to absorption of incident photons;[74,75] (iii) cathodoluminescence where photons are emitted due to an excitation from incident electrons;[76] and (iv) energy loss spectroscopy (EELS), where the energy lost from an electron due to an LSPR excitation is measured.[77]

The far-field methods instead rely on probing the signal in the far field, which means that they are inherently diffraction limited. The techniques to study properties of single nanoparticles in the far field include: (i) scattering micro spectroscopy, where light scattered from a single nanoparticle is measured; and (ii) photothermal imaging used to study absorption of light.[78] Because of the strong light-matter interaction resulting from LSPR active nanoparticles, scattering measurements of individual plasmonic nanoparticles can be done using relatively simple equipment, consisting of a traditional optical microscope with a dark-field condenser. Additionally, as long as individual nanoparticles are separated by a larger distance than the diffraction limit (i.e. a few 100 nm), they can be seen as individual bright spots in a microscope, which allows for several individual particles to be measured simultaneously.[23,24,79,80] However, a significant limitation of single particle spectroscopy based on scattered light is the fact that scattering from a particle scales as r^6, as shown in eq. 2.3. This means that as the particle size is decreased the scattering signal will diminish quickly, resulting in difficulties to investigate single nanoparticles with a size smaller than around 50 nm. To overcome this, the previously discussed INPS scheme can be utilized, by e.g. placing the small and thus weakly scattering nanoparticle close to a larger, better scatterer to act as signal amplifier.[23,25]

In this thesis, I have used a method called dark field scattering spectroscopy (DFSS) to study the spectral response of individual nanoparticles both in the direct and INPS variants. The working principle of DFSS will be discussed further in chapter 6.

3 Catalysis

In 1835 Jöns Jacob Berzelius, then secretary of the Royal Swedish Academy of Sciences, published a report where he defined catalysis as a process where a substance influenced a chemical reaction without itself being affected.[81] This definition built on several reports where by letting a chemical reaction proceed in vicinity of certain materials one could influence the reaction itself. Since then, this rather vague definition has been refined and a more recent one was proposed by W. Ostwald as: "*A catalyst is a substance which affects the rate of a chemical reaction without being part of its end product*".[82] As for further definitions, if the catalyst and the reacting species are in the same state of matter or in a different state of matter, the process is categorized as homogenous or heterogeneous catalysis, respectively. Homogenous catalysis is primarily important in biological systems, where large macromolecules, such as enzymes, perform a plethora of different homogeneous catalytic reactions to keep an organism alive. When it comes to man-made catalytic processes at the industrial scale involving both gas and liquid phase reactants, heterogeneous catalysis using a catalyst in the solid-state is the key technology.

The use of heterogeneous catalysis has had an enormous impact on the evolution of human society and today we have catalysis to thank for fuels, polymers, clean air and medicines.[7] Another very notable discovery, solely based on a heterogeneous catalytic process, was made in 1909 when Fritz Haber found a way to bind atmospheric nitrogen into fertilizers (ammonia), effectively preventing mass starvation and making it possible for the world population to grow in an unprecedented way.[8,83–85] Although industrially useful, the full description of how a catalyst actually works under realistic conditions remained a mystery for several decades, and to some extent is still an open question.

This chapter is intended to give a brief background to what heterogeneous catalysis is, why it is important, and how research in the field of catalysis is typically carried out.

3.1 The principle of catalyst function

The working principle of a catalyst can be summarized as a system that offers energetically more favorable reaction pathways for a chemical process, without itself being consumed.[7]

A typical chemical reaction involves breaking and forming of bonds between molecular species to transform chemical compounds into new configurations. To this end, if two species, A and B, can react through a chemical reaction to form an energetically favorable species C, it may seem intuitive to assume that that reaction would happen spontaneously. However, in many cases, although thermodynamically allowed, the reaction of A + B → C is inhibited because there are some *intermediate* molecular configurations that are energetically unfavorable, causing the reaction to proceed extremely slowly. This is illustrated in Figure 3.1, where the solid lines represent the potential energy of the reactants A and B, and of the product C, as well as of the energy barrier in-between them. The latter is a consequence of the intermediate elementary reaction steps, which require energy, the so-called activation energy (E_a), in order for the reaction to proceed. This energy has to be supplied externally, usually via heat (k_BT), where k_B is the Boltzmann

constant and T is temperature. The probability for the reaction to proceed can be described by the Boltzmann distribution ($P \propto e^{-\frac{E_a}{k_B T}}$). From this relation one can immediately see that, if E_a is high and T is moderate, the probability for the reaction to proceed is very small. To circumvent this situation, a catalyst is used, which, as indicated by the dotted lines in Figure 3.1, can introduce a new pathway for the reaction that involves different elementary steps with lower activation barriers. In this way it can effectively change the energy landscape in a fashion that less activation energy is required and an increased reaction rate at lower temperature can be achieved. An important thing to note is that in the described scenario the start and end products in both cases are the same. Thus, the thermodynamics are unaffected because the catalyst only changes the kinetics of the reaction. However, if there are several competing chemical reactions available, a catalyst can, in principle, be tailored to only target one of them and thus be used to control the ratio of end products. This can be used to increase selectivity for otherwise unfavorable reactions.

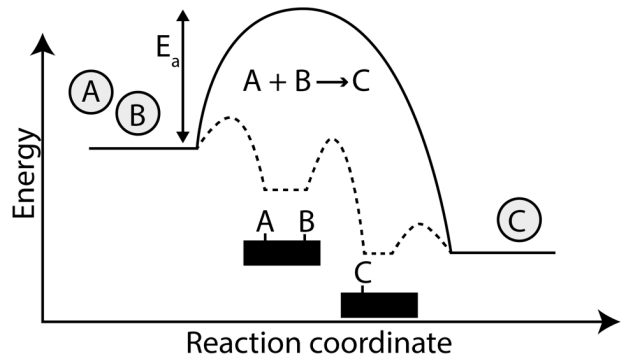

Figure 3.1. **Catalyst principle.** Energy diagram for a chemical reaction in the presence (dotted line) and absence (solid line) of a catalyst for the reaction between species A and B forming the product C. E_a is the activation energy needed for an uncatalyzed reaction. The intermediate steps along the dotted line correspond to typical intermediate reaction steps, namely adsorption of gas species (A & B) onto the surface, surface reaction to form C and finally desorption of C to the gas phase.

3.2 Heterogeneous catalysis

In heterogeneous catalysis the typical catalyst is a solid material where the surface atoms are catalytically active. When a solid material is terminated by a surface, the outermost atoms have fewer neighboring atoms to form bonds with than the ones in the bulk, that is, they have a lower coordination number. These under coordinated surface atoms thus have unsaturated bonds that rather easily can form bonds with a molecule approaching the surface through what is known as chemisorption. When such bonds are formed between a surface and a molecule, the original electronic structure (chemical bonds) of the adsorbing molecule (as well as of the surface) will be modified, potentially causing intra-molecular bonds to weaken or break, thereby forming new surface-bound species that can participate in a catalytic reaction along a new reaction pathway with lower activation barriers.

Typical heterogeneous catalysts consist of metallic or metal-oxide structures that have nanoscale dimensions (~3-4 nm) to, for instance, maximize their surface to volume ratio to minimize material cost per active reaction site. However, as previously mentioned already in the nano-optics chapter, the down-scaling of materials to the nanosize regime can also severely change their original physical and chemical properties. This effect is of great importance also for catalysis were nanoparticles provide modified physical structures, electronic structure and therefore changed reactivity compared to their bulk counterparts.[8] Efforts have been taken to explore the differences in reactivity imposed by changing from single crystalline (bulk like) to supported nanoparticles exposing a wider range of facets, corners and edges.[86] Additionally, theoretical models to understand kinetics on nanoparticles have also been explored and revealed significant differences to the bulk case.[87,88] Yet another complication is the fact that each individual nanoparticle will differ from the next. This has been experimentally addressed on model catalytic reactions to reveal that, in the case of hydrogen adsorption in Pd, differences in shape, size and grain structure indeed changes the properties of supported metal nanoparticles.[23,24,89–91]

3.2.1 How to study heterogeneous catalysts

Although used and studied for more than a century, catalytic surface reactions and the state of the active catalyst are still very challenging to experimentally investigate under realistic reaction conditions. This can be explained by the fact that the reaction steps occur very rapidly and that real catalyst materials are complex, typically consisting of nanoparticles of active catalyst material dispersed on chemically complex matrixes of (oxidic) support material to create a large specific surface area for reactions to take place (*materials gap*). Furthermore, industrial catalysts are operated at ambient pressure or above, which is challenging for a wide range of experimental techniques that in principle can be used to study catalytic reactions (*pressure gap*).

In one way to get around the complexity problem, scientists traditionally have replaced the complex real catalysts with simplified so-called model systems, where the chemical and structural complexity is drastically reduced. Historically, such model systems consisted of macroscopic single crystalline surfaces and they were investigated using surface sensitive techniques such as Low energy electron diffraction (LEED) X-ray photoelectron spectroscopy (XPS), Auger electron spectroscopy (AES), scanning tunneling microscopy (STM) and molecular/ion beam scattering.[92] Other spectroscopic, microscopic and diffraction techniques for characterizing catalysts include X-ray diffraction (XRD) used to determine crystallinity of samples, electron microcopy (SEM and TEM) to investigate structure and morphology, infrared spectroscopy that is widely used to determine surface species, Raman spectroscopy, UV-vis spectroscopy, Nuclear magnetic resonance (NMR) and methods based on X-ray absorption (XAS, EXAFS, XANES) that often rely on synchrotron light to maximize their resolution.[7]

The techniques above that rely on electrons, molecules or ions traveling to/from the sample to a detector are traditionally limited to use under ultra-high vacuum (UHV) conditions due to scattering of particles by gas molecules. Therefore many studies of catalyst materials have been done at UHV conditions, i.e. at pressures 10^5 - 10^{11} orders of magnitude lower than the operational pressures of commercial catalysts or the three-way catalyst in an automotive vehicle. Despite this pressure gap, knowledge gained from

studying ideal surfaces under UHV conditions has in some cases correctly predicted reaction rates in an industrial process (and thus bridged the pressure gap).[93] However, sometimes, going from UHV conditions to pressures used in practical catalyst applications (above 1 bar) is accompanied by changes in mechanisms.[7,10,14] Since several of the above methods, e.g. IR spectroscopy, XRD and synchrotron based X-ray absorption techniques (XAS, EXAFS, XANES) are not limited by pressure they can bridge pressure gap and are used to characterize real catalysts *in-situ.*[94] Furthermore, as part of intense efforts to bridge the pressure gap, techniques like high pressure STM and AFM, ambient pressure XPS (APXPS) and environmental TEM (ETEM) are today being developed.[10,14,95–98] To this end, scientist have used differential pumping to enable XPS[99] and TEM[100] under pressures in the mbar range which has been used to e.g. shed light on the heavily debated active phase of Rh and Pd during CO oxidation by use of APXPS.[94]

When it comes to the material gap, part of the difficulty is instead that each individual nanoparticle has its own unique size, shape and microstructure, giving rise to ensemble averaging effects as soon as larger samples are measured. To avoid this, scientists have turned to developing single particle sensitive techniques to measure both structure and activity related information[15], with some examples being tip enhanced Raman spectroscopy to measure activity[101], X-ray microscopy to measure catalyst morphology and composition[102] and TEM to look at microstructure.[103]

In parallel with the evolution of experimental techniques, the ability to use theoretical modelling of materials from first principles using mainly density functional theory (DFT)[104] has brought about the ability to predict material properties and chemical reactions, which has resulted in a massive surge in the field of computational chemistry[105]. Using DFT paired with other computational techniques one can today simulate nanoparticles with realistic sizes (<5 nm) in an ab-initio manner,[87,106] which in combination with the improved downscaling of nanofabrication techniques, means that we are closer than ever to bridging the materials gap.

Microreactors

As another aspect of the ongoing efforts to bridge material and pressure gaps to gain deeper insights into catalytic reactions, the concept of "microreactors" has been introduced. Since the nanoreactor concept developed in this thesis essentially is the downscaling of the microreactor concept to the nanometer scale, in this section, I will give a brief overview of what microreactors are and why they are useful. For a more comprehensive description I refer the reader to one of the rather recent review articles or textbooks that exist on the subject.[107–109]

The term microreactor in catalysis research refers to a reactor with at least one dimension in the submillimeter range. Such a reactor can look like a conventional tubular reactor with very small dimensions[110] but more often considers reactor designs that utilize microfabrication techniques to make the reactor.[107,108,111,112] Benefits of using reduced dimensions compared to conventional reactor design include improved heat transfer, faster diffusion times, precise control of mass transport to the active catalyst, increased safety due to lower volume of potentially hazardous compounds and the ability to do more precise in-line analysis of the reaction products.[107–109,113,114] In addition, reducing the reactor dimensions reduces the amount of catalyst material needed to result in a

measurable amount of reaction products, making it possible to use precise top down nanofabrication methods such as electron beam lithography (EBL) to make model catalyst nanostructures.[115]The materials used to make microreactors are typically based on their compatibility with microfabrication techniques such as electron beam lithography, photolithography and reactive ion etching, as well as with the need for chemical inertness. Hence, the materials of choice are therefore typically Si and SiO_2. Using combinations of Si and SiO_2 makes it possible both to make channels of varying size as well as integrating sensors and heaters to make "reactor on a chip" devices that can withstand temperatures up to 400-500°C.

Microreactors also allow access for different *in situ* characterization methods on very small amounts of catalyst. For example, the microreactor platform developed by Henriksen et al[115] enables characterization of Pt model catalysts down to active areas as low as 15 μm^2 using mass spectrometry and by using optically transparent materials also facilitates photo catalysis experiments[116] and optical characterization.[117] More recently, the same platform has been adapted to gracing incidence small-angle x-ray scattering (GISAX)[118] and similar Si-based microreactors have been demonstrated to be compatible with *in-situ* IR-thermography,[119] Raman spectroscopy,[13,120] X-ray diffraction, absorption and microscopy,[102,119] UV-vis spectroscopy[121] and FTIR[122] characterization of the active catalyst.

Microreactors also play an instrumental role in the recent attempts to increase the spatial resolution of *in situ* catalyst nanoparticle characterization down to the atomic level. Specifically, by adapting the microreactor concept to transmission electron microscopy (TEM), it has become possible to monitor individual catalyst nanoparticles with atomic resolution in real time and at reaction conditions.[13,103,123] This has generated new fascinating insights into Pt nanoparticle reshaping in an oscillatory manner during CO oxidation reaction[13] as well as dramatic oxidation of Co nanoparticles.[124]

Despite these unique possibilities offered by in situ TEM in microreactors with respect to monitoring the catalyst itself during reaction with atomic resolution, even this approach still has a number of limitations. For example, simultaneous analysis of reaction products stemming from individual nanoparticles is still far out of reach. As demonstrated recently, when *in situ* single nanoparticle TEM characterization is combined with analysis of reaction products, the latter is obtained from a large ensemble of nanoparticles that is considered to homogenously cover the whole length of the 320 μm wide reactor, hence, only reflecting heavily ensemble-averaged properties.[103] In other words, it is still very difficult to establish direct structure-function correlations at the single nanoparticle level. A second key limitation of the TEM approach is that only one nanoparticle can be monitored and characterized at the time since the electron beam has to be focused on that particle. As the consequence, it becomes impossible to monitor several individual nanoparticles simultaneously, meaning that one cannot directly compare the behavior of individual catalyst in the same experiment but only in sequence. Since nanostructures are dynamic during reaction and thus change with time due to, for example, sintering, this is a significant limitation.

3.2.2 The CO oxidation reaction over a Pt catalyst

To give an example of a catalytic reaction that both is of relevance for my thesis and probably one of the most studied model reactions in catalysis, I will here discuss the oxidation of carbon monoxide (CO) by oxygen (O_2) occurring over a metallic catalyst. It follows the reaction scheme

$$CO + \frac{1}{2}\, O_2 \longrightarrow CO_2 \tag{3.1}$$

Below 700°C the reaction does not take place spontaneously in the gas phase but only proceeds efficiently on metallic surfaces such as Pt, Pd, Rh and Cu.[7] Here I will focus on CO oxidation over Pt, which has been extensively studied since the 1970's[95] due to the importance in the automotive industry where removal of CO from the exhaust is vital. Based on surface science UHV studies the reaction mechanism can be described to be of the Langmuir-Hinshelwood, according to the following four elementary steps that are also illustrated in Figure 3.2. [7,125]

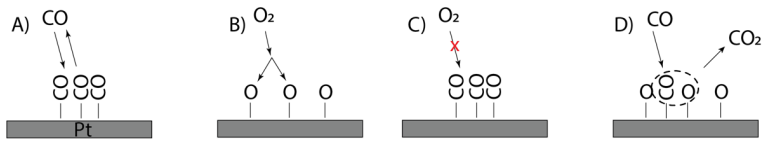

Figure 3.2. **Catalytic CO oxidation on Pt.** A) Adsorption and desorption of CO. B) Dissociative adsorption of O_2. C) Preabsorbed CO inhibits O_2 adsorption. D) CO adsorption next to previously adsorbed O species and resulting surface reaction to form CO_2.

Reversible adsorption of CO, Figure 3.2A, and dissociative adsorption of O_2, Figure 3.2B, on the Pt surface

$$CO + * \rightarrow CO* \tag{3.2}$$

$$O_2 + 2* \rightarrow 2O^* \tag{3.3}$$

Surface reaction (Figure 3.2 D)

$$CO^* + O^* \rightarrow CO_2^* + * \tag{3.4}$$

And lastly, desorption of CO_2 (Figure 3.2D)

$$CO_2^* \rightarrow CO_2 + * \tag{3.5}$$

where * indicates an available site on the surface or an adsorbed species if used as a superscript. In this reaction scheme, the so-called rate determining step is the surface reaction between chemisorbed CO and O, for which the rate can be expressed in terms of surface coverages of O (Θ_O) and CO (Θ_{CO}) as

$$r = \mathrm{k_{rx}}\Theta_O\Theta_{CO} \tag{3.6}$$

where k_{rx} is the rate constant. From eq. 3.6. it is clear that, to maximize the reaction rate, Θ_O and Θ_{CO} should be as high as possible and equal. Consequently, it is important to briefly discuss the dependence of Θ_O and Θ_{CO} on Pt surfaces on gas phase composition, temperature, pressure and state of the catalyst surface. At low temperature, CO species adsorbed to a Pt surface tend to form a densely packed surface layer while O species form a more open structure since they adsorb in threefold coordinated sites.[8,125,126] Because O_2 adsorbs dissociatively, it requires several free neighboring sites and consequently this process is inhibited if the CO coverage exceeds a critical value Figure 3.2C. The main consequence of this is that a surface exposed to a steady-state flow of gas phase CO and O_2 will quickly be covered by adsorbed CO that inhibits O_2 adsorption and hence suppresses the reaction. This is known as CO poisoning.[127] To overcome this problem, temperature can be increased, resulting in a higher desorption rate of CO, while O_2 desorption is much less affected. The increased CO desorption will allow gas phase O_2 to compete for the freed adsorption sites and Θ_O is increased. A practical consequence of the above is the so-called "cold start problem" of the automotive three-way catalytic converter, i.e, that it is not functioning efficiently before it has been heated up.

The CO poisoning effect results in two distinct reaction regimes, i.e. the poisoned regime (high Θ_{CO} and $\Theta_o \cong 0$) where the rate depends negatively on CO concentration, and the low CO coverage regime where the rate increases linearly with increased CO concentration. The transition between these two regimes can occur in a narrow CO:O_2 mixing range and gives rise to a dramatic change in reaction kinetics known as *kinetic phase transition.*[128] Close to the kinetic phase transition point the two kinetic regimes are almost equally stable for the same mixing ratio of O_2 and CO, which gives rise to a bistability that induces hysteresis. In other words, the reaction rate is determined by the direction in which the mixing ratio is changed, i.e. whether the CO concentration is increased or decreased.

The change in surface coverage with respect to CO and O has also been shown to cause a structural reorganization of the topmost atomic layer(s) of the Pt surface.[7] In turn, this structural reorganization changes the adsorption and reaction dynamics, which eventually again results in a change in surface coverage, etc. Hence, spatial and temporal oscillations of the reaction rate as well as the surface structure can occur, as famously demonstrated by Ertl and co-workers on single crystal surfaces at low pressures.[8,129] More recent studies made at ambient pressures have revealed even more dramatic changes including surface oxidation[10,95] and roughening,[12,130] as well as nanoparticles dynamically changing shape.[103] These studies have also shown indications that the previously suggested Langmuir-Hinshelwood mechanism might be accompanied by a so called Mars-van Krevelen (MvK) mechanism in which a CO molecule reacts with a pre-formed surface oxide[95] instead of just chemisorbed O-species.

4 Nanofluidics

Nanofluidic systems offer unprecedented possibilities to confine, control and study fluid flow at the nanoscale in and around nano sized objects. Although different fields have studied nanoscale flow for a long time, the name nanofluidics is rather recent, as it emerged in the early 2000's in the footsteps of microfluidics.[17] The transition from micro- to nanofluidics can be partially attributed to the improvements in the field of nanotechnology that allow for more precise characterization, as well as better control of smaller structures. Traditionally, nanofluidics is reserved to describe fluidic systems where at least one dimension is on the order of 1-100 nm. However, sometimes the definition stretches into the μm-regime in what is called "extended nanofludics",[131,132] which allows for a wider range of nanometric objects to be studied, e.g. single cells or macromolecules such as DNA.

Because nanoscale phenomena related to flow are inherent to many fields, nanofluidics is naturally interdisciplinary. To illustrate this, Figure 4.1 present disciplines that incorporate knowledge on nanofluidics in some way, together with some relevant applications.[17]

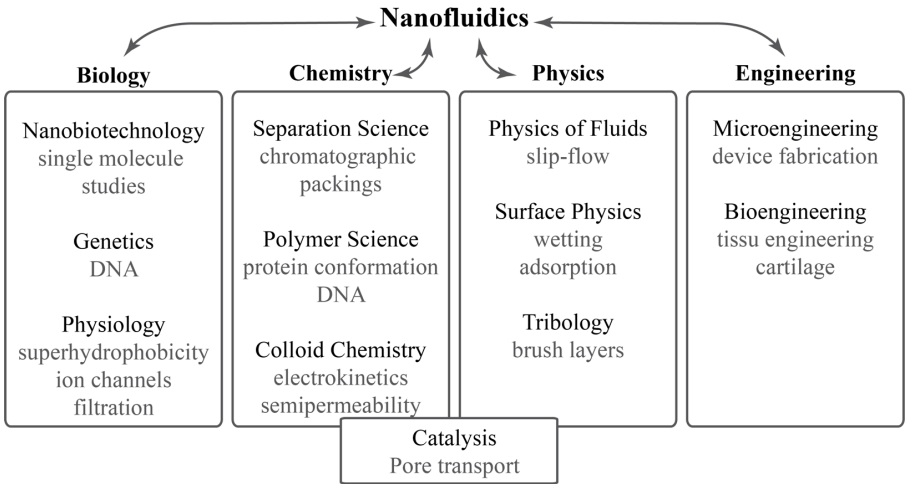

Figure 4.1 Research disciplines related to nanofluidics within a number of relevant subjects. (Adapted from [17]).

Although nanofluidics can be considered as an evolution of microfluidics, it is important to note that the distinction between the two stretches far beyond the difference in size. When scaled down to < 100 nm, new phenomena start to emerge, which opens up possibilities not only to study smaller samples, but also to investigate new scientific territories. Due to the extreme confinement, the physical behavior of fluids in nanofluidic structures like nanochannels can differ significantly compared to the bulk case. This can be explained by the characteristic length scales of the fluid such as the hydrodynamic

radius, the Debye length and the electronic double layer being on the same scale as the confining structures. To this end, a selection of phenomena that have been observed and investigated with the help of nanofluidics are nonlinear transport resulting in concentration polarization,[133,134] ion-current rectification[135,136] and changes in the properties of liquids.[137–139] A multitude of additional studies of the properties of liquids confined at the nanoscale exist and I refer the interested reader to one of many review articles on the topic.[131,132,140–142] Of more direct relevance for the work presented in this thesis, is another aspect of nanofluidics, that is, the possibility to enable precise mass transport down to the level of individual (macro) molecules that can be delivered to specific sites to be investigated or detected. This precise control has been applied in nanoparticle/molecular sieves[143,144] as well as to reshape molecules as demonstrated by e.g. stretching of DNA to measure the length of a DNA molecule[145] or for DNA mapping.[146]

One important technological aspect of nanofluidics that is essential to the applications presented in this work is the ability to functionalize the *inside* of the nanofluidic system with functional nanostructures as exemplified in Figure 4.2.

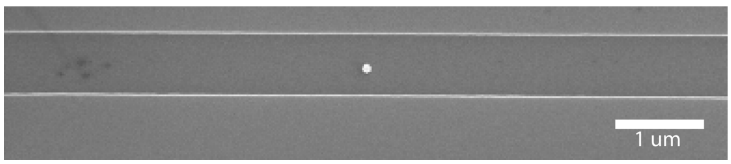

Figure 4.2. **Functionalized nanochannel**. SEM micrograph of a nanoparticle (~100 nm) placed inside a 100 nm deep and 900 nm wide nanochannel.

The emerging capabilities to do so have been proposed as the key to bring nanofluidics from the more fundamental physics oriented stage to a more application oriented regime.[131] Nevertheless, due to the small dimensions, selective functionalization of nanofluidic systems is a major challenge. For example, since one of the main approaches to fabricating nanofluidic systems is to use lithography-based nanofabrication techniques[147] where the nanofluidic structures are etched into a substrate and sealed by a lid that is chemically bonded to the substrate, any functionalization inside the channels that requires nanoscale precision has to be done *prior to* the bonding. Furthermore, the positioning of a nanoscale object inside another nanoscale structure is by itself non-trivial and requires very careful alignment. Hence, to the best of my knowledge, prior to my own contribution to this field presented in this thesis, there existed only one successful example, for the functionalization of the inside of a nanofluidic system with nanoparticles.[148] The authors demonstrated a method to place nanoparticles as well as seal the chip using a room temperature bonding process. Furthermore they used the patterned structures for molecular functionalization within nanochannels. In contrast, I am mainly interested in the optical readout capabilities of functionalizing nanofluidic systems with nanostructures to shed light on nanoparticle changes taking place on individual particles during catalysis and I am using a nanofluidic system for the first time to confine a gas rather than a liquid.

5 Nanofabrication

In his now legendary talk entitled "There's plenty of room at the bottom", Richard Feynman in 1959 envisioned the benefits of being able to manipulate physical objects on the atomic level. Back then the electron microscope had already been invented and provided the possibility to image objects with nanometer resolution. However, the art of making and manipulating the world at the nanoscale had not yet been explored. Now, almost 60 years later, we have undoubtedly come a long way where each and every one of us has one of the miniaturized computers envisioned by Feynman in our pockets.

The progress in nanofabrication and nanocharacterization has given rise to the field of nanotechnology that bridges chemistry, physics, biology and engineering. It has not only resulted in a deeper understanding of the world but also made it possible to make new materials. Furthermore, many of the techniques that I have used to make and characterize samples in this thesis are direct results from the developments in nanotechnology during the past decades. In this chapter I will go through the main principles of these techniques.

5.1 Lithography

To be able to define different structures on top of or in a substrate, a masking layer can be used to prepare the underlying layer for processing. In nanofabrication, these masks are often made from polymer materials that can be lithographically patterned using different techniques. Often patterns are generated by exposure to radiation that induces a chemical change, followed by a chemical processing step that selectively removes part of the polymer mask. When exposing the mask to radiation the maximum resolution (minimum size) of the pattern that can be made is set by the wavelength of the exposing radiation. Therefore different techniques are used depending on the desired structures. In general, a lithography process can be divided into the three main steps summarized in Figure 5.1. They are:

1. **Coating** the sample with a mask material, typically a polymer, by spin coating.
2. **Exposing** the mask to radiation (photons or electrons).
3. **Developing** the exposed mask, resulting in a patterned mask that can be used for further processing.

These three steps will be further explained in this section, followed by examples of what can be done to further process the sample, once the lithographic mask is in place.

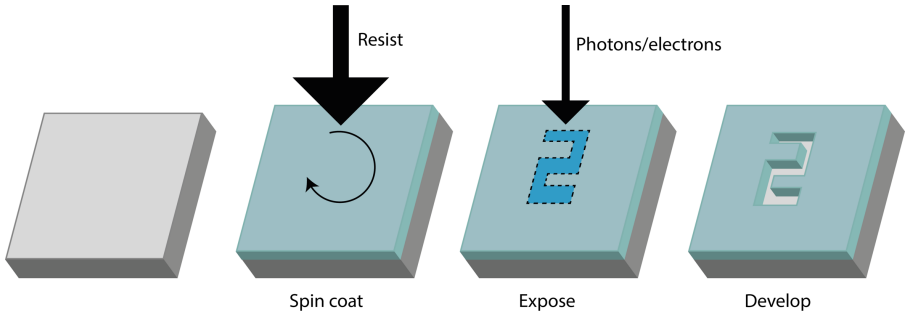

Figure 5.1**. Main Lithography steps**. The three main steps of making a mask for further processing are: (i) applying a resist, typically by spin coating a polymer material; (ii) exposing the resist using light or electrons to chemically alter the resist layer; (iii) developing the resist, effectively removing the exposed areas to make the underlying substrate accessible for further processing.

5.1.1 Spin coating

The first step of a lithographic process is to apply the temporary masking layer to the substrate that is being processed. Typically, this mask is a so- called (photo-)resist consisting of a specific polymer that is spin-coated onto the substrate. Spin-coating is a process where a spinning substrate is used to apply a thin uniform polymer layer with a well-known thickness. The process is rather simple as a droplet of the resist material is applied to a horizontally placed sample, followed by acceleration up to a spin-rate of a few thousand rpm depending on the resist, as well as the desired thickness. Spinning continues for about a minute followed by a baking step were the sample is heated up to evaporate any remaining solvent from the polymer film.

5.1.2 Optical lithography

Optical lithography is based on selectively exposing parts of a light sensitive polymer to UV- or visible light. The exposure results in a chemical change that is followed by dissolving either the exposed or the non-exposed area in a solvent, in what is known as positive and negative lithography, respectively. The light exposure is commonly done either through a pre-patterned photomask or by focusing a laser beam onto the resist to "write" the desired pattern. Practically, the main difference between using a pre-patterned photomask or a laser writer is that the photomask can be used several times and the exposure process is quick (less than 30s), while the laser exposure scales linearly with the size of the exposed area resulting in around 1h exposure time for a 10x10cm pattern with a modern machine. However, if the pattern is expected to be different for each exposure the laser writer is much more convenient since the pattern can be changed by only modifying a file instead of having to make a new photomask.

5.1.3 Electron beam lithography

Electron beam lithography (EBL) is used when the resolution needed surpasses the capabilities of optical lithography due to the diffraction limit, and it is the process with the highest possible resolution available today. The reason is that, due to their small wavelength, electrons can be focused to a much smaller spot than photons. Hence, they

can be used to make patterns with a resolution on the order of a few nanometers.[149] The working principle of an EBL system is that an electron beam is focused onto a substrate by a series of magnetic lenses that both shape the beam, as well as control its position. A modern EBL system typically relies on a thermal field emitter using Zr/O/W to supply a stable electron beam at variable currents.[150]

The resolution limit in EBL comes not from the actual wavelength of the electrons that is in the picometer range when using a 100kV acceleration voltage. Instead it is dictated by how the electrons travel through the resist as it is exposed. Since the electrons will scatter both from the resist material itself and from the underlying substrate it results in an area larger than the beam size itself being exposed. In addition, secondary electrons with energies up to 400 eV are generated as the primary electrons are slowed down when traveling through the resist material. These electrons have a traveling distance of 5-10 nm, which is one of the major causes for the limited resolution. These effects also have to be taken into account when structures are written close to each other since exposing one of the structures can lead to partially exposing the neighboring structures as well. This is called the proximity effect.[151]

The basic steps of an EBL process follow the scheme illustrated in Figure 5.1 and are as follows: 1) Spin-coat a substrate with a polymer resist that is sensitive to electron exposure. 2) Align the sample using predefined alignment marks to calibrate the machine to the positions of the sample. 3) Irradiate the sample with an electron beam at the positions defined by the user. The irradiation will cause the exposed areas to either soften or harden depending on the chosen resist. 4) Develop the exposed mask in an appropriate developer liquid causing the exposed (or un-exposed) areas to dissolve, leaving a patterned resist for further processing.

Although EBL is the process of choice in nano- and micro fabrication when the highest resolution is needed, it does not come without drawbacks. The major one is the long writing time that makes large area patterning for industrial purposes extremely costly or even impossible.

5.2 Etching

Removal of material can be used as a means of patterning a surface. In micro- and nanofabrication, different types of etching are used to remove specific materials. Etching methods can be roughly grouped in two main categories: wet etching and dry etching. The former relies on liquid (wet) chemicals to remove materials, and the latter on gaseous molecules (often in the form of ionized plasma) to physically remove material and/or chemically react with the substrate. Another important classification of etching processes can be made between isotropic etching methods that etch with a similar rate in all directions and anisotropic etching that etches differently, depending on etching direction (Figure 5.2).

5.2.1 Wet etching

Thanks to years of development by chemists there exists a lot of knowledge about how different materials react with other chemical species. This knowledge is today readily accessible in various databases and allows one to rapidly identify which combination of materials that could be used to effectively protect and etch different parts of a sample.[152]

Depending on the system, wet etching can be isotropic or anisotropic, e.g. depending on the crystalline orientation of a substrate.

5.2.2 Dry etching

Reactive ion etching (RIE) is the most common dry-etching method and makes use of reactive ions to etch away different materials. Depending on the choice of ionic species, different materials can be etched selectively. When designing an etching process, it is important to consider the relative etch rates between the material used as a mask and the material that is to be etched. These rates can be found in the literature.[152] RIE can also make use of physical etching by accelerating ions towards the substrate to remove material due to the physical impact of the ions.

To initiate the etching process a sample is typically placed inside a vacuum chamber with a controlled gas environment. A plasma of the chosen gas is ignited, creating a mix of atoms, ions and free electrons in the chamber. Due to their higher mobility, the free electrons will quickly accelerate towards the anode of the chamber and the positive ions left behind will therefore start accelerating towards the cathode, where the sample to be etched is placed. Upon impact, these accelerated ions will physically knock out atoms from the substrate, thereby causing an etching effect. At the same time, the highly reactive ions will react with the substrate material creating volatile gaseous species that are pumped out of the chamber. In this process, one can also tune the degree of chemical (reactive) and physical etching to achieve more or less anisotropic results, as illustrated in Figure 5.2.

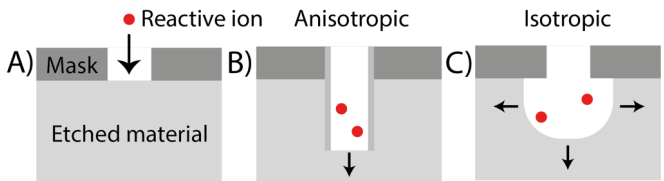

Figure 5.2. **Reactive ion etching.** A) A reactive molecule is ionized and accelerated towards the substrate by an electric field. Depending on the process parameters an anisotropic B) or isotropic C) etching profile can be achieved. To achieve deep anisotropic etching one can utilize a polymer to protect the sidewalls, as schematically depicted by the grey regions that cover the walls of the trench in B).

One of the more specialized processes used to achieve deep anisotropic etching into Si is known as the Bosch process or as deep reactive ion etching (DRIE).[153] The process works by cycling between an etching step and a passivating step that protects the surface from the reactive gases. The first step in the process is to passivate all surfaces with a polymer that is resistant to the reactive gas mixture used in the etching step. The second step involves etching by both sputtering and reactive ions. The role of sputtering is to remove the protective polymer film. Because this sputtering effect is controlled by an applied forward voltage it is directional and thus only etches surfaces that are perpendicular to the direction of the accelerated ions. The protective polymer will thus remain only on the sidewalls of previously etched trenches (Figure 5.2B). In regions where the protective polymer has been removed, the reactive ions will etch the substrate. As the result, a trench that is being etched will be etched only in the direction normal to the sample surface,

resulting in strongly anisotropic etch profiles. These two steps are cycled until the desired etching depth is achieved.

In my work reactive ion etching was used to make the micro- and nanochannel systems in paper I and III. For the nanochannels etched into SiO_2, a Fluorine based RIE process was used. For the deeper microchannels, as well as for the inlet holes that were etched into Si, DRIE was used. RIE with O_2 was also used to selectively remove polymer resist materials in the HCL process to make nanostructures for paper II.

5.3 Thin film growth

Another way of patterning surfaces is to add material instead of removing. Here, different ways of adding materials will be discussed in terms of growing thin films.

5.3.1 Thermal oxidation

One way of growing a thin film onto, for instance, Si is by thermally oxidizing it in a controlled way to form a thin film of SiO_2. This thermal oxidation can be achieved in two ways called wet or dry oxidation, depending on if the oxidation is done in the presence or absence of water, respectively. The corresponding reaction schemes look as follows:

$$Si\ (s) + O_2(g) \rightarrow SiO_2(s) \text{ or}$$

$$Si(s) + 2H_2O(g) \rightarrow SiO_2(s) + 2H_2(g),$$

where g and s correspond to solid and gas phase, respectively.

The oxidation of a clean Si wafer takes place in a furnace with a temperature of typically 800 – 1200 °C, were the wafer is exposed to an oxidizing atmosphere containing O_2 or H_2O. The relationship between oxide thickness and time is a function that is strongly dependent on temperature, pressure and what crystal orientation is to be oxidized. The equations governing this process are well known and online tools for process planning are readily available.[154,155]

5.3.2 Thin film deposition

There exist several ways to grow materials onto a substrate with thickness control at the nanometer scale.[156] Here, I will briefly discuss the thin film deposition methods relevant to this work.

Chemical vapor deposition (CVD) relies on inducing a chemical reaction on the surface of a sample. This is done by introducing reactants in the gas phase in a vacuum chamber, where they adsorb to the sample surface and react to form the deposited material. CVD is typically used to deposit oxides or nitrides. For example SiO_2 can be deposited through a reaction between SiH_4 and N_2O.

Physical vapor deposition (PVD) relies on the condensation of vaporized atoms and clusters on a substrate. Materials that are deposited using PVD are often metals, metal oxides or nitrides that are vaporized either through thermal evaporation or by sputtering atoms from a source/target that is placed in vacuum together with the substrate that is to be coated.

In *sputtering* the atoms or clusters are created by bombarding a target of the desired material with ions (typically Ar) that knock out target species. The ions are generated

using plasma, and are accelerated towards the target using an electric field. Some of the ejected atoms will then travel through the chamber and hit the substrate where they are deposited.

In contrast, *evaporation* relies on heating the source material until the vapor pressure is high enough that atoms exit the source and travel (in vacuum) through the deposition chamber to eventually condensate when landing on the sample surface. Heating of the target is done either resistively or by an electron beam. Because an electron beam can be tuned to very high energies and focused into a small spot size, it can create extremely high target temperatures and is thus used to evaporate materials with high melting temperatures such as tungsten, carbon or alumina. In contrast to CVD, deposition done by evaporation is very directional. This results in highly anisotropic deposition profiles where only areas in direct line of sight of the target will be covered.

In this thesis, evaporation based PVD was used for the growth of the nanostructures in all appended papers, as well as for the fabrication of the resistive heaters on the nanoreactor chips.

5.4 Hole mask colloidal lithography

One challenge with conventional lithography is to pattern large areas (~cm^2) while still maintaining nanometer precision. Using conventional optical lithography, the resolution is limited by the diffraction limit, and structures below a few 100 nm are not attainable. At the same time, the lower resolution attained with EBL is limited by the fact that exposure time scales with an increase in exposed area. A solution to these limitations is to use self-assembly based methods that rely on nanostructured objects arranging themselves on a surface, meaning that the process is naturally parallel rather than serial. One such process that uses colloidal suspensions of nanostructures for patterning is colloidal lithography (CL).[157] In this chapter I will specifically discuss a variant of CL that has been developed at Chalmers and is known as Hole-mask colloidal lithography (HCL).[158]

HCL utilizes charged polystyrene (PS) beads that are self-assembled on an oppositely charged substrate, resulting in a quasi-randomly spaced scarce monolayer of PS on the underlying substrate.[158] The fabrication steps are presented in Figure 5.3 and are as follows: 1) The substrate is cleaned with acetone, isopropyl alcohol (IPA) and methanol, each solvent followed by immersing the beaker in an ultrasonic cleaning machine for 3 minutes. 2) Poly(methylmethacrylate) (PMMA) is spin coated on the substrate followed by baking on a hotplate at 170°C for 10 minutes to evaporate any remaining solvent. 3) A short etch by oxygen plasma is performed on the PMMA to reduce the hydrophobicity of the substrate. 4) Poly(diallyl dimethylammonium) (PDDA) in water solution drop coated on to the surface for 40 seconds, followed by rinsing in deionized water. This creates a thin positively charged layer on top of the PMMA. 5) A dispersion of polystyrene (PS) particles in water is drop coated on to the surface for 3 minutes, followed by 20 seconds rinsing in deionized water. The concentration of the PS solution can be varied to be able to control the surface coverage of the final structures.[159] The PS particles have a negative surface charge and therefore attach to the positively charged PDDA surface, while at the same time repelling each other. This results in coverage with a typical nearest neighbor distance but without long range order. 6) A thin film (around 20nm) of

a material of choice (typically Cr or Au) is deposited by evaporation onto the surface covered with PS. 7) Tape is placed on top of the covered surface. When removed, the tape will strip the PS particles, leaving a mask with holes defined by the PS particle diameter where the underlying PMMA is exposed. 8) Oxygen plasma etching through the holes in the metal mask transfers the hole pattern into the underlying PMMA. In this step, longer etching time results in a larger undercut, meaning that the PMMA is etched parallel to the substrate surface to create a hole that has a larger diameter than the hole in the mask. 9) By evaporating materials through the holes, structures are formed on the substrate surface with a shape determined by the hole. 10) After completing the evaporation, the mask is removed by dissolving the PMMA using acetone in a lift-off step. This results in removal of all material that is attached to the PMMA layer, leaving only the material that is deposited directly on the substrate.

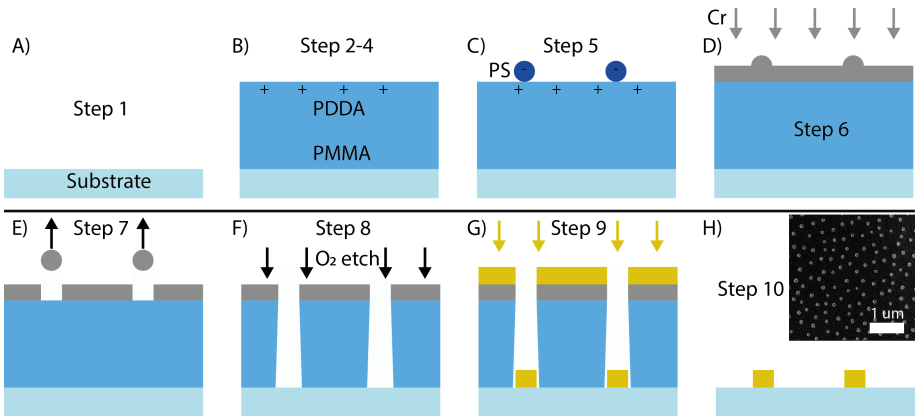

Figure 5.3. **Hole-mask colloidal lithography fabrication steps.** A) Substrate is cleaned. B) PMMA is spin coated on the substrate and the surface is made positively charged by adsorption of a polyelectrolyte (PDDA) layer. C) Polystyrene beads with opposite charge to the PDDA are self-assembled on the surface from aqueous solution. D) The mask layer of Cr or Au is deposited by PVD. E) Tape is used to strip away the PS beads, leaving holes in the metal mask. F) Holes are etched through the PMMA layer using reactive ion etching. G) The desired structure material is deposited by PVD. H) The PMMA is dissolved resulting in the top layer being lifted off, leaving the substrate patterned with nanoparticles. The inset shows an SEM image of an array of 100 nm Au disks fabricated using HCL.

5.4.1 Shrinking hole colloidal lithography

A variation of the HCL process known as Shrinking Hole Colloidal Lithography (SHCL) has been developed to be able to create complex nanostructures, such as multimers of different size and material.[160] SHCL utilizes the fact that the PMMA layer can be under-etched in step 8 (Figure 5.3F), and that by depositing material at an angle, several particles can be placed consecutively through the same mask in a self-aligned way. Because each deposition will cause a slight shrinking of the hole in the mask, consecutive depositions will furthermore result in slightly smaller structures. An example of the SHCL process is presented in Figure 5.4, were the first material (Au) is deposited at an angle placing the disk slightly off center. Following this deposition, a layer of Cr is deposited at a high

angle (45°) while rotating the sample, resulting in the Cr only getting deposited on the PMMA walls, as well as on top of the Au mask-layer. The purpose of this layer is to only shrink the size of the hole without leaving any material on the substrate. The third deposition is subsequently done at a small angle opposite to the angle used for Au, resulting in a smaller Cu particle placed next to the Au. This technique was used to create the Au-Cu heterodimer arrays for plasmonic sensing of Cu oxidation in paper II.

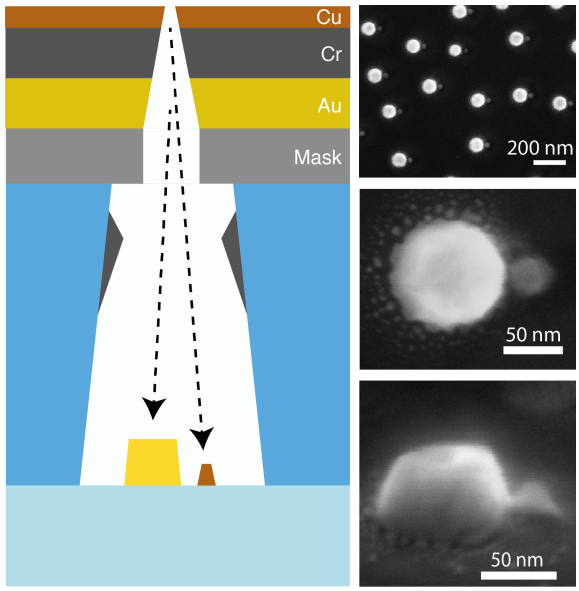

Figure 5.4. **Shrinking hole colloidal lithography.** By depositing material at an angle and utilizing the fact that the hole shrinks, multimer structures can be fabricated from an HCL mask. First, Au (yellow) is deposited, followed by Cr (dark grey) that is deposited at an angle while rotating the sample so that the material ends up on the PMMA walls. Lastly Cu (orange-brown) is deposited at a small angle through the smaller hole. To the right, three SEM images of Au-Cu heterodimer(s) are presented, showing the obtained structures viewed from the top (top two) and from the side (bottom).

6 Characterization techniques

To make my work possible I have used many different characterization techniques to get information about my samples. The methods have been used both to look at the structure of samples on the nanoscale and to characterize the state and reactivity of nanoparticles during chemical reactions. This chapter summarizes the most used techniques and go through their basic mode of operation.

6.1 Mass spectrometry

Mass spectrometry (MS) is an analytical method used to measure the molecular or atomic composition of a sample. For this thesis I used it to analyze gas phase composition in what is known as residual gas analysis (RGA). A MS works by ionizing molecules and separating them, depending on their specific mass to charge ratio (m/z). Ionization of the molecules can be achieved in different ways, e.g. by exposing them to high-energy particles (electrons or ions), thermally, by electric fields or by laser irradiation. After ionization, the ions are separated based on their mass to charge ratio by the mass analyzer. The separation can be done using different methods that all rely on the fact that the trajectory and velocity of an ion accelerated in an electric field depends on its mass and charge. After the mass separation the species with the selected mass hit a detector that is used to count the number of ions, typically using a Faraday cup or an electron multiplier. In this chapter, I will briefly discuss the basic principle of a mass analyzer used in mass spectrometry. For a more detailed description I refer to the literature.[161]

6.1.1 Mass analyzer

The kinetic energy (E_k) gained by an ion with charge q when moved through a field with a voltage U is:

$$E_k = \mathrm{Uq} = Uze \tag{6.1}$$

where e is the electron charge and z is an integer corresponding to a number of electrons. This can be translated to the velocity gained by the ion with mass m_i

$$v_i = \sqrt{\frac{2ezU}{m_i}} \tag{6.2}$$

which shows that the velocity gained by a heavier ion is lower than by a lighter one if they both have the same charge. Hence, the simplest type of mass separation technique is based on the time it takes for an accelerated ion to travel a certain distance and is known as a time of flight (TOF) mass spectrometry. A different approach to separating masses is the *quadrupole mass spectrometer (QMS).* In a QMS the mass separation takes place by injecting an accelerated ion into a mass filter that consists of four parallel rods under a combined DC and AC potential, with the same potential applied to an opposing pair of rods (Figure 6.1). An ion traveling through the mass filter will thus have a trajectory dictated by the applied potential and can be described by solving the Mathieu

equations.[161] If the parameters are tuned in a way that results in the ion not hitting any of the rods it will pass through the filter and is detected by the detector. The conditions for achieving this are very precisely defined, which allows a QMS to separate ions by their m/z ratio.

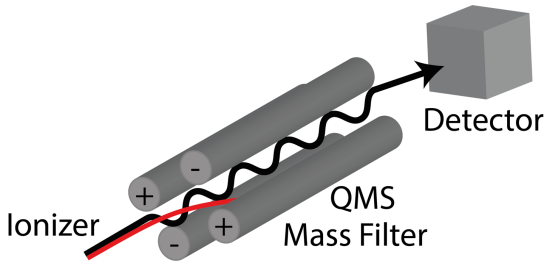

Figure 6.1 **Quadrupole mass filter**. A combined DC and AC potential is applied to four parallel rods and determine the trajectory for ions travelling between them. Depending on the m/z ratio an ion will either hit one of the rods (red line) or pass through (black line) the filter and reach the detector.

In both TOF and QMS mass filters the ratio m/z is what identifies the specific ion. This means that singly ionized molecules with the same original mass will behave identical in the mass filter. Hence, two different molecules with the same mass, e.g. N_2 and CO, have the same m/z-ratio 28 and cannot be distinguished. As a way to get around this problem one can analyze additional masses corresponding to fragments of the original molecule, also known as cracking patterns. In the above example, CO could separate into C an O during ionization, resulting in m/z ratios 12 and 16 also being present in the mass spectrum, which is not the case for N_2. Additionally, multiple ionization events can occur, generating ions with higher charge that in turn will be detected as lower mass species. Therefore, care must be taken by the user of a mass spectrometer to ensure that the correct species is measured.

6.2 Electron microscopy

One of the most widely used techniques to image matter on the nanoscale is electron microscopy. The two main sub-techniques of electron microscopy are scanning electron microscopy (SEM)[162] and transmission electron microscopy (TEM).[163] The main difference between the two methods is that SEM utilizes a raster-scanned beam and electrons traveling backwards from the sample are monitored. In contrast, in a TEM, electrons transmitted through the sample are used for imaging. As a consequence of this, the sample has to be thin enough to let electrons travel through. In TEM the incident beam can be either wide, illuminating the whole sample at once, to generate the image, or it can be swept over the sample as in the SEM in what is known as scanning transmission electron microscopy (STEM). Between TEM and SEM, the former achieves the highest spatial resolution and can even be used to image individual atoms, while SEM has a typical resolution of around 1 nm.

In this work SEM has been heavily used to image samples during and after fabrication, as well as to characterize the samples after being exposed to e.g. chemical reactions. Because TEM requires more advanced equipment and samples fabricated on thin (<100

nm) substrates it has been used less frequently and only for more specific tasks where the resolution of the SEM was not sufficient.

6.2.1 SEM

In a SEM, a focused electron beam is raster-scanned over the sample, while different detectors are used to analyze the emitted or back-scattered radiation in the form of electrons or photons. There are several different types of interactions between the primary incident electrons and the sample, among which elastic and inelastic electron scattering are the two most important ones for SEM image generation.[162] The elastically scattered electrons, known as backscattered electrons (BSE), have lost little to no energy during their interaction with the sample and thus have the same energy as the incident beam. The yield of BSE is strongly dependent on the molecular weight of the material and thus gives good chemical contrast of the sample. Examples of this contrast can be seen in most SEM images presented in this thesis, e.g. Figure 5.4, where the heavier metals (Cu & Au) appear brighter than the underlying Si.

Secondary electrons (SE), on the other hand, are electrons that have been ejected from an atom in the sample due to an inelastic interaction with the primary beam. The kinetic energy of these electrons is typically less than 50 eV, which limits their travel distance through a solid material to a few nm. Therefore, SE can only originate from the upper most fraction of the sample and they are used to get topographic information.

When an electron is emitted by an atom due to interaction with the primary electron beam, the empty energy level will quickly be filled by an electronic transition of an electron in a higher energy state. The energy lost in this transition can result in emission of a photon in the X-ray range that can be detected. Since the possible electronic transitions of each element are unique, one can map the energies of these emitted X-rays to get compositional information of the sample through what is known as energy dispersive X-ray spectroscopy (EDS or EDX). One of the limitations of SEM is that the sample generally has to be conductive. This is to avoid charges building up on the sample surface resulting in deflection of the incident electron beam. For non-conducive samples this problem can be alleviated by e.g. covering the sample with a thin film of a metal prior to imaging.

6.3 Optical characterization

The optical analysis of nanoplasmonic structures is one of the main themes of my work and different types of optical characterization methods have been utilized to study both ensembles and individual nanostructures.

6.3.1 Spectrophotometry

Spectrophotometry is used to characterize how a material interacts with light in the UV-visible-NIR range of the electromagnetic spectrum. When shining light onto a sample, the light-matter interaction will result in three possible events: transmission, scattering or absorption. To measure the extent of these processes a spectrophotometer can be used. The working principle of a spectrophotometer is that an incident beam with a well-known intensity is irradiated onto a sample. By measuring the intensity ($I(\lambda)$) as a function of wavelength for light that has interacted with the sample and comparing it to the incident light intensity ($I_0(\lambda)$), the transmission spectrum can be attained as $T = \frac{I}{I_0}$. The extinction

spectrum, defined as the sum of absorption and scattering, is related to the transmittance, T, as $E = 1 - T$ and thus corresponds to how much light has been absorbed or deflected (scattering) from traveling in forward direction. As discussed in chapter 2, plasmonic nanoparticles in the commonly used size regime (~100 nm) exhibit both scattering and absorption. Therefore, to be able to distinguish between light that has been scattered and absorbed, additional measurement methods have to be employed, e.g. measuring absorption alone using an integrating sphere.

6.3.2 Dark field scattering spectroscopy

Dark field microscopy is a technique that is used to quantify light scattered from the sample surface, rather than relying on light absorption as in more common bright field microscopy. To achieve dark-field illumination the specimen of interest has to be illuminated in such a way that the direct incident light is not transmitted or reflected into the objective of the imaging light path. This is typically achieved by illuminating the sample from a sufficiently high angle, such that incident or reflected light is not collected by the objective. Hence, the so-called dark field image that is obtained is created only by light scattered (or emitted e.g. through fluorescence) by the sample, as illustrated in Figure 6.2.

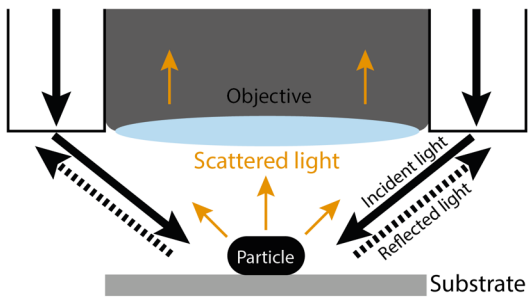

Figure 6.2. **Dark field illumination.** By illuminating the sample at a high angle the reflected incident beam does not end up in the imaging path (objective) and only scattered light is collected.

Plasmonic nanoparticles, although much smaller that the wavelength of visible light, scatter light strongly at their plasmonic resonance. Hence, they feature a scattering spectrum that is highly dependent on the material, shape, size and electronic surroundings of the nanoparticle, as discussed in chapter 2. Accordingly, single metallic nanoparticles down to a size of a few tens of nanometers can be resolved as distinct individual scattering point-sources in a dark-field optical microscope, Figure 6.3A. By focusing them onto a spectrometer with a grating that separates the light into its wavelength constituents it is thus possible to spectroscopically analyze the scattered light of individual plasmonic nanoparticles, Figure 6.3B, in what is known as dark field scattering spectroscopy (DFSS).

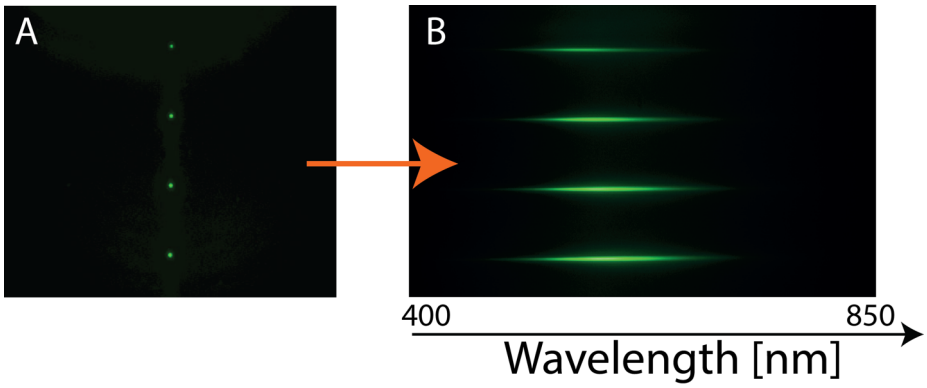

Figure 6.3. **Dark field scattering spectroscopy.** A) Dark field scattering image of 4 nanoparticles seen through a 50X objective of an optical microscope. B) The same four particles resolved as a function of wavelength by inserting a grating in the light path.

To correct for scattering from the substrate, as well as for the wavelength dependence of the lamp and the detector, a corrected scattering spectrum is obtained as

$$I_{scattering} = \frac{I_{particle} - I_{background}}{I_{lamp}} \qquad (6.3)$$

where particle, background and lamp stand for the raw scattering counts measured over an area containing a particle, without a particle and the corresponding lamp spectrum, respectively.

For my work spectroscopic studies of both ensembles and single particles was used. Often the experiments take place over long times (several hours) and the optical response is recorded continuously by gathering optical spectra at pre-defined time steps.

7 Nanofluidic Chip for Single Particle Catalysis

A major part of this thesis has been focused on designing, fabricating and characterizing a novel type of nanofluidic chip that (i) enables mass transport in the gas phase to and from individual nanoparticles, (ii) provides optical access to the inside of the channels to enable single particle dark field scattering spectroscopy, (iii) provides temperature control up to 650 K and (iv) that can be connected to a QMS for residual gas analysis of reaction products created inside the nanofluidic system. In this chapter, I will explain in detail the working principle of these nanofluidic chips, as well as how they are nanofabricated.

7.1 Gas phase nanoreactor setup

To bridge the previously mentioned pressure and materials gaps in heterogeneous catalysis we designed and built an integrated gas-phase nanoreactor system connected to a QMS (Figure 7.1). In this system, the nanofluidic chip (Figure 7.1B,C) at its core enables controlled gas phase mass transport to and from individual and optically accessible catalytic nanoparticles, while simultaneously monitoring reaction products exiting the reactor using the QMS. To accomplish this the Si/SiO_2 based nanofluidic chip is connected to a customized macroscopic ambient pressure gas flow control system based on off-the-shelf Swagelok components on the inlet side, and on the outlet side it is connected to an ultra-high vacuum (UHV) chamber equipped with a high-end QMS (Hiden HAL/3F PIC). For this purpose, a customized sample holder was designed (Figure 7.1B) and is discussed in detail below. This sample holder is then mounted on the motorized stage of an upright optical microscope (Nikon Eclipse LV150) to enable DFSS of the catalyst nanoparticles inside the nanochannels by means of a spectrometer (Andor 193i) equipped with and EMCCD camera (Andor iXon Ultra 888). This arrangement enables the simultaneous monitoring of the catalyst (surface) state at the single nanoparticle level and to correlate it with reaction product formation to derive structure-function correlations. Below, I will discuss the different key components of this setup in detail.

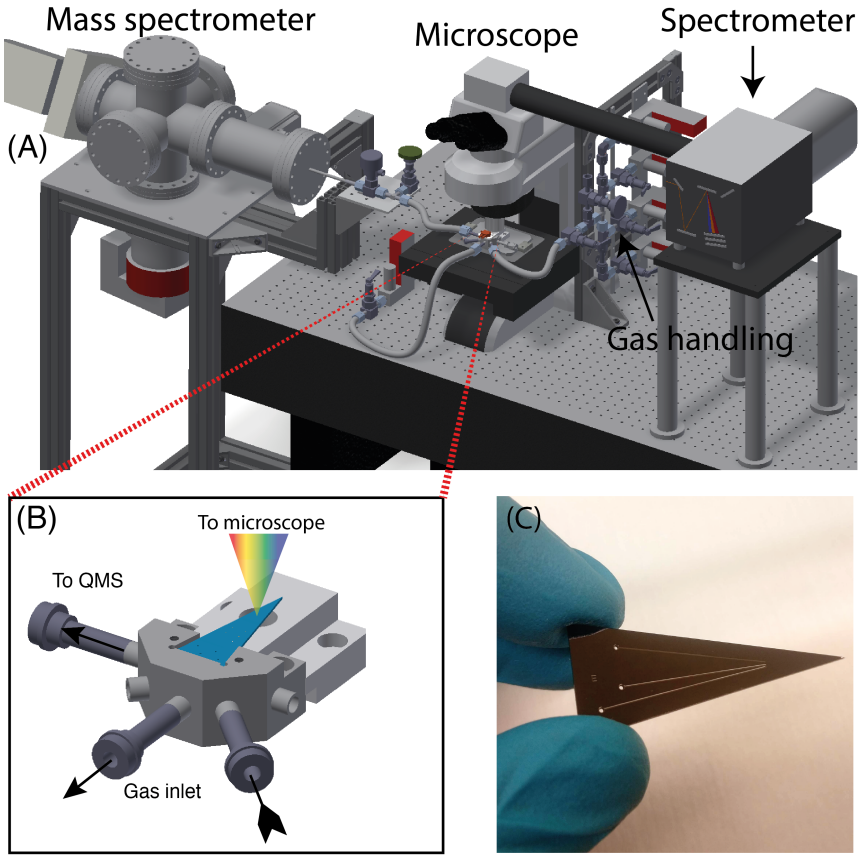

Figure 7.1. **The Nanoreactor setup**. A) Schematic depiction of the complete nanoreactor instrument. The nanofluidic chip is mounted in the tailor-made chip holder that connects it to the gas managing system, as well as to the QMS. The chip holder is mounted on the motorized stage of an upright microscope equipped with a dark-field objective and coupled to a spectrometer equipped with an imaging EMCCD camera shown to the right. B) Zoom-in of the nanoreactor chip holder that connects the chip (blue) to the gas supply, as well as the QMS. The chip is mounted such that the tip, where the nanofluidic structures are located, is accessible by the optical microscope for DFSS analysis of individual catalyst nanoparticles placed inside. C) Photo of a nanoreactor chip where the microfluidic channels and the inlet holes are seen.

7.1.1 Nanofabrication of the Nanofluidic chip

The general nanofabrication scheme for the chips is summarized in Figure 7.2 with the main steps as follows: 1) Oxidizing a p-type Si wafer by thermal oxidation to a desired oxide thickness (typically 100-300 nm). 2) Defining nanochannels into the oxide using electron beam lithography (EBL) and reactive ion etching to etch SiO_2. 3) Defining larger microchannels using optical lithography, etching through the SiO_2 using RIE or a HF-based wet-etch followed by DRIE to etch into the Si. 4) Making holes through the Si

wafer to enable connecting an external gas or liquid supply from the face of the chip. The holes were made in the same way as the microchannels but etching using DRIE for a longer time. 5) Fabricating a heater by patterning a mask on the back of the chip with optical lithography and depositing a 10 nm Cr layer, followed by 100 nm Pt, using electron beam evaporation. 6) Fabricating nanoparticles in the nanochannels by defining a mask using EBL and depositing the desired material using electron beam evaporation. 7) Sealing the chip by fusion bonding[164] a glass wafer to the top of the Si/SiO_2 chip at 550°C. This process relies on the fact that when two perfectly clean and flat SiO_2 surfaces come in contact at this temperature, covalent bonds are formed between the two surfaces. 8) The chip is cut into the desired shape using a dicing saw.

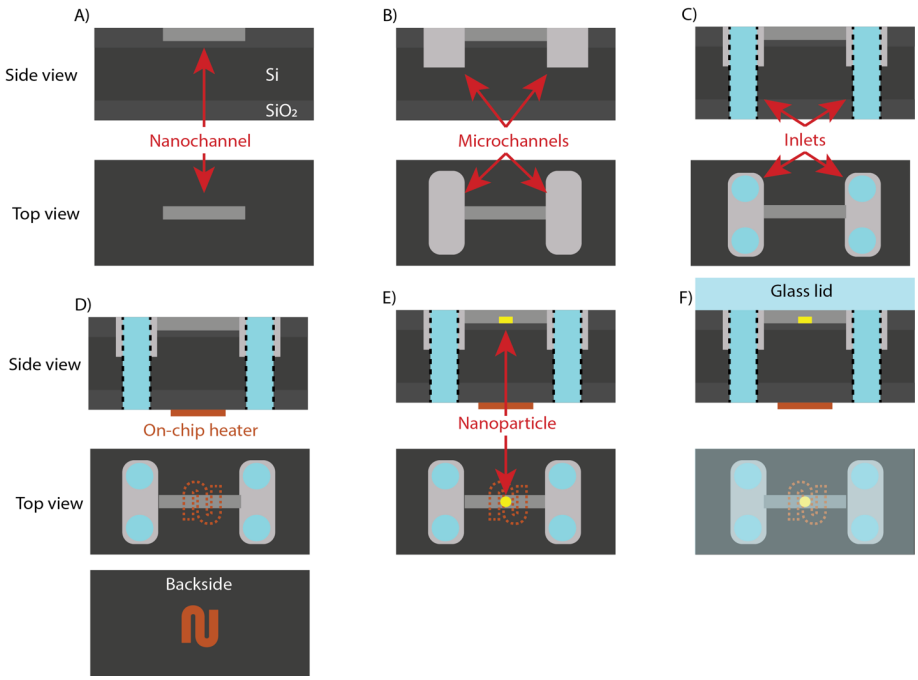

Figure 7.2. **Main nanofabrication steps for the making a nanofluidic chip for single particle catalysis.** A) Nanochannels are fabricated into 200 nm thermal oxide on a Si wafer by EBL followed by RIE. B) Larger microchannels are then made by optical lithography followed by RIE/DRIE through both the SiO_2 and into the Si. They connect to the nanochannels. C) Inlet holes to the microchannels are defined by optical lithography and etched using DRIE through the Si wafer. D) (If needed) a resistive heater is placed on the back of the chip by Pt evaporation through a mask defined by optical lithography. E) Nanoparticles are fabricated inside the nanochannels by evaporation through a mask that has been patterned by EBL. F) A glass lid is fusion bonded on top to seal the channels.

7.1.2 Nanoreactor chip holder and gas supply

To connect the nanoreactor chip to the macroscopic world, we designed and manufactured a chip holder, which enables (i) mounting of the chip on the stage of an upright optical microscope to facilitate optical spectroscopy, (ii) controlled supply of gas

at up to 10 bar pressure on the inlet side and (iii) the effusion of the reaction products from the nanoreactor into an UHV chamber equipped with the QMS. 3D drawings of the chip holder with and without a mounted chip are presented in Figure 7.1B & Figure 7.3, respectively.

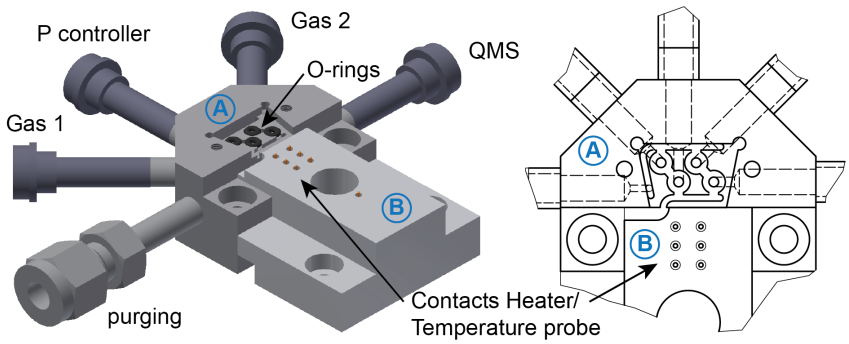

Figure 7.3. **Chip holder.** 3D (left) and 2D (right) depictions of the chip holder, illustrating the 5 gas ports used for gas handling and the 6 electric contacts used to set and measure the temperature of the nanoreactor. A and B in the figures indicate parts that are fabricated in stainless steel and ceramics, respectively.

The chip holder is machined from stainless steel and equipped with Swagelok VCR connections. Furthermore, electrical connection to the chip for heating and temperature readout is enabled by six gold plated electronic spring pins embedded in a machinable ceramic block (B in Figure 7.3). To minimize air leaks, perfluoro elastomer (FPM) O-rings are placed at the interface between the fluidic chip and the sample holder in micromachined grooves that are surrounded by an Ar flow system to continuously flush the O-rings with inert Ar gas from the purging inlet in Figure 7.3. The gas inlet connections of the holder connect to an array of four mass flow controllers (MFCs – Bronkhorst) that are used to determine the gas mix entering the chip on one side, and a pressure controller on the opposite side to control the pressure of the gases at the inlet of the nanoreactor chip. Using this arrangement and by varying the flow rate set at the MFCs used, the time to fully exchange the microfluidic system at the inlet side from one gas composition to another can be controlled. A typical flow of 10 ml/min results in a time for gas change in the range of ~5 minutes, with the gas exchange in the macroscopic gas lines connecting the MFCs with the chip holder as the main determining factor.

The nanoreactor chip itself is held in place on the chip holder by a stainless-steel block clamping it from above. On top of this block, a water-cooled copper heat exchanger is installed to actively cool the part of the chip that is mounted in the holder to minimize the heating of the chip holder upon operation of the on-chip heater described in detail below. This is important since it turned out that indirect heating of the chip-holder increased the leaking through the O-rings and thus had a negative impact on the performance of the system.

7.1.3 Microfluidic system of the nanoreactor chip

The microfluidic gas supply system on the inlet side is designed in a U-turn fashion (Figure 7.4A). Gases enter the chip through the bottom connector marked “In”, flow in

the direction indicated by the arrows and exit through the outlet hole, where an on-line pressure controller is used to set the upstream pressure. The dimensions of the U-turn are chosen such that they enable gas flow rates on the order of 1-10 ml/min, without significant pressure drop. This yields dimensions on the order of 200 μm width and 50 μm depth or bigger. This microfluidic inlet system connects to the nanochannels at the tip of the U-turn, which means that the pressure set in the microchannel determines the inlet pressure in the nanoreactor, which in turn determines the flowrate through the nanofluidic system. On the outlet side of the chip the nanochannels connect to a second microfluidic system with the same dimensions (upper channel of Figure 7.4A), which is directly connected to the UHV system with the QMS. Hence, *all* gases that have passed through the nanoreactor are collected here for residual gas analysis.

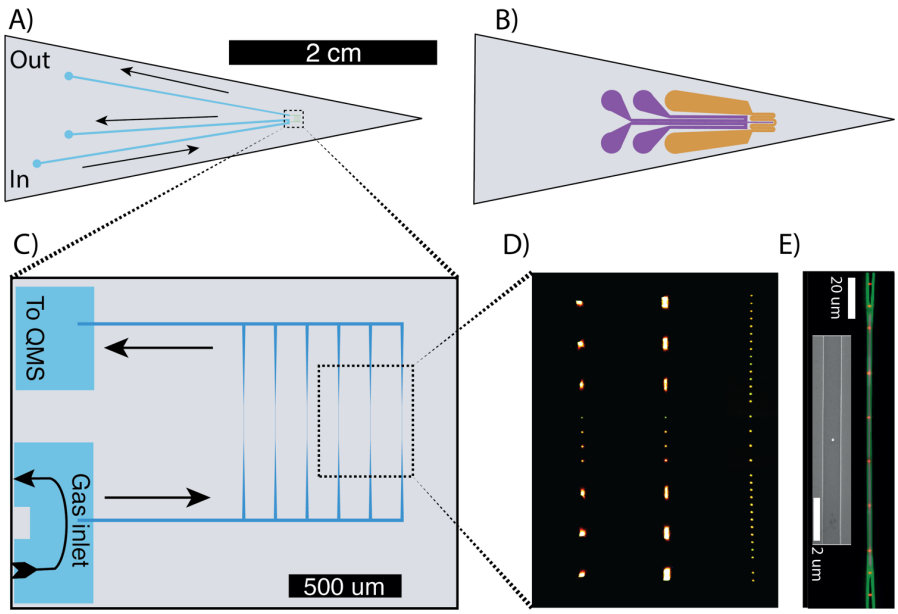

Figure 7.4. **Nanofluidic Chip.** A) Schematic depiction of the used chip with the microfluidic system shown in light blue. The arrows show the direction of the gas flow both on the inlet (high pressure) side and on the outlet (low pressure towards QMS) side. B) The backside of the chip, which is decorated with the resistive Pt heater (yellow) and thermometer (purple). C) Zoom-in on the nanofluidic part where the nanoreactor consists of 6 parallel channels decorated with catalyst nanoparticles of choice. D) Dark-field microscopy image of three nanoreactor channels decorated with different numbers of catalyst nanoparticles. The right channel is filled with a single row of 36 individual Au/Pd nanoparticles with dimensions ~120 nm. The two left channels instead contain dense patches with regular arrays (pitch 200 nm) of identical nanoparticles. Since the particle-particle distance is smaller than the diffraction limit, they can't be resolved individually. In the center region, all three channels have four differently sized particles (100nm, 110 nm, 120 nm, 130 nm) which appear as individual dots with slightly different color and scattering intensity due to their different size. E) Artificially colored dark-field microscopy image of a single nanochannel (green) containing a row of individual nanoparticles (red dots) together with a SEM micrograph inset of a single nanochannel decorated with a single catalyst nanoparticle.

7.1.4 Nanofluidic system of the nanoreactor chip

The nanochannels are the core of the nanoreactor since the catalyst nanoparticles are placed inside them. They are designed in such a way that they enable the accurate control of the reactant flow to the nanoparticles. Specifically, the dimensions of the nanofluidic channels determine the flow rate and number of reactant molecules supplied at the position of the catalyst nanoparticles. Hence, the nanochannels can be tuned to either yield a higher flow by making them wide and short or a lower flow by making them long and/or narrow. In the chip presented in Figure 7.4C the dimensions of the channels are 100 nm depth with a width of 10 μm at the wider parts down to 400 nm in the narrow, central, parts. This yields a molecular flow rate of approximately 5×10^{11} molecules/s for an inlet pressure of 2 bar.

Since in our setup all gas exiting the nanoreactor is directly fed into the UHV system with the QMS, the flow rate and thus the dimensions of the nanochannels also determine the base pressure in the vacuum chamber which, to ensure safe operation of the QMS, is ideally kept below 10^{-8} mbar. To further characterize and quantify gas flow through our system, we have executed both indirect measurements and employed theoretical fluidic models, as detailed below.

7.1.5 On-chip Heater

To enable precise temperature control of the reaction volume of the chip (i.e. the nanochannel region), an on-chip resistive heater and four-point probe thermometer were microfabricated on the backside of the nanoreactor chip. The heater design is presented in Figure 7.4B where the yellow part corresponds to the heater and the purple part to the thermometer. We chose Pt as the material for the device due to its stability and reliable resistance to temperature relationship that is close to linear in a wide temperature range.[165]

The specific heater design in terms of geometry was adapted to ensure that the heating is focused to an area corresponding to the nanochannel part of the reactor chip and that the temperature readout is from the center of the heater. The heater is controlled by driving a current through the Pt film using an external power supply. Temperature readout is achieved in a four point probe fashion[165] by monitoring the resistance of the Pt film, which changes in a well-defined way as a function of temperature.[166] To calibrate the temperature-resistance relationship for our device it was immersed in an oil bath heated to a series of temperatures, while simultaneously logging the resistance of the sensor. The data were then fitted to a Callendar-Van Dusen polynomial with the form[167]:

$$R(T) = R_0(1 + \alpha T + \beta T^2) \qquad (7.1)$$

were R_0 is the resistance at 0°C, α and β are the coefficients and T is the temperature in °C. The obtained data and corresponding fit based on equation 7.1 are presented in Figure 7.5 and yielded $R_0 = 150\ \Omega, \alpha = 0.0021\ \mathrm{K}^{-1}$ and $\beta = -6.5 \cdot 10^{-7}\ \mathrm{K}^{-2}$.

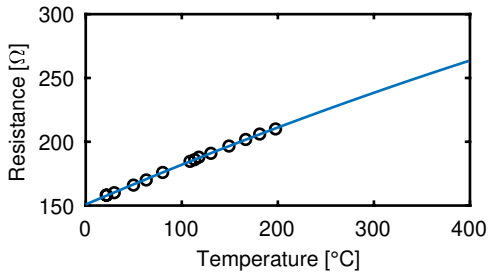

Figure 7.5**. Calibration curve for the on-chip heater.** Black circles correspond to the measured resistance at a given temperature and the blue line to the fitted function based on eq. 7.1, used to extrapolate the response at higher temperatures.

The heater, as well as the four-point probe thermometer, are connected to a temperature control unit (Lakeshore 335) that acts as a proportional–integral–derivative (PID) regulator that can set and maintain a given temperature. With the current design, a working temperature range of 20 – 375°C can be achieved with a rather quick response time of <10 s in the range from RT to 375 °C. Although cooling is passive, due to the small size of the chip in combination with it being mounted to a cooled metal block, going down from 375°C to <30°C takes less than 20 s.

7.1.6 Dark-Field Scattering Spectroscopy of individual catalyst nanoparticles

For DFSS measurements, the nanoreactor chip is placed under an upright optical microscope (Nikon LV150) equipped with a 50X EPI-illumination dark-field objective. Connected to the microscope is an imaging spectrometer (Andor i193) equipped with an EMCCD (Andor iXon Ultra 888) that enables both imaging and spectroscopy of the particles placed under the microscope. To ensure the particles are held in place under the course of experiments, that can span over several days, a motorized stage (Märzhäuser Wetzlar SCAN) with a built-in feedback loop is used.

In the nanofluidic channels, the nanoparticles can be seen as bright spots together with light scattered from the surrounding channel walls. This is shown in Figure 7.4E that displays an image taken through the microscope where the channel walls have been artificially colored green and the particles colored red for clarity. To minimize background signal and to be able to isolate the optical response of the particles, the scattering from the walls is eliminated by installing an aperture in the illumination light path, as illustrated in Figure 7.6. In this way, by blocking incident light perpendicular to the channel, scattering from the channel walls can be efficiently suppressed (Figure 7.6B). The individual scattering spectra of the nanoparticles can then be resolved by means of DFSS, as described in chapter 5.

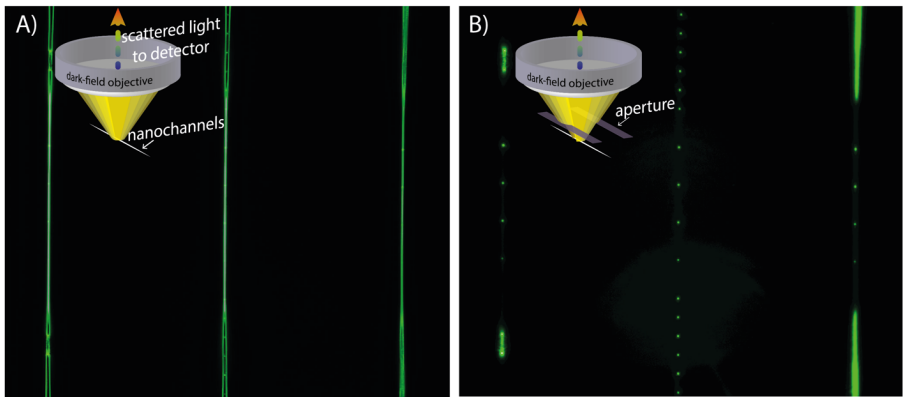

Figure 7.6. **Dark field microscopy of particles in nanochannels.** A) Dark field image of 3 nanochannels containing nanoparticles obtained without aperture blocking light incident perpendicularly to the nanochannel direction. B) Same as A) but with an aperture inserted to block light incident perpendicularly to the nanochannels, effectively eliminating scattering from channel walls and making the individual nanoparticles visible.

7.1.7 Quadrupole Mass Spectrometry

The outlet of the chip is directly connected to the UHV chamber hosting the QMS via stainless steel tubing. To enable movement of the chip under the microscope, flexible (Swagelok) tubing is used which also serves to minimize vibrations translated from pumps to the microscope stage. The gas lines as well as the vacuum chamber hosting the QMS can be heated to avoid gases sticking to the surfaces and thus avoid being detected. To minimize background signal and maximize the sensitivity, the base pressure of the QMS chamber is 10^{-10} mbar. Upon operation of the nanoreactor, it rises to approximately 5×10^{-9} mbar, depending on the chip design and the pressure set at the inlet. The residual gas detection in the chamber is performed with a triple filter quadrupole mass spectrometer equipped with a pulsed ion counting detector (Hiden HAL/3F PIC) and a gold-plated ion source.

7.2 Characterization of the nanoreactor chip

7.2.1 Flow through the nanochannels

The gas flow rate though the nanochannels is determined using a method inspired by the work of Henriksen et al.[115] In this experiment, the driving force of the flow through the nanochannels is determined by the pressure difference between the high and low pressure side of the channels. Hence, by holding the inlet side at constant pressure (at or above ambient pressure) while pumping the outlet side to below 0.001 mbar, the pressure difference between the two sides, $\Delta P = P_{in} - P_{out}$, can be estimated as only depending on the high pressure side since $P_{in} \gg P_{out}$. The experiment was conducted by establishing a known pressure of Ar on the inlet side of the chip and monitoring the resulting pressure increase over time on the outlet side where the gases enter a known closed volume. This is schematically illustrated in Figure 7.7A, where the left side of the figure corresponds to the constant pressure inlet side and the right side to the closed

volume where the pressure (P) is monitored. Presented in Figure 7.7B is the resulting pressure (P) as a function of time for three different inlet pressures (2, 3 and 4 bar). By utilizing the ideal gas law, the increase in pressure can be translated into a molecular flow as

$$\dot{N} = \frac{V}{k_B T}\frac{dP}{dt} \tag{7.2}$$

where $\dot{N}$ is the molecular flow entering the volume, $V = 4.95\times10^{-5}\ m^3$ is the known volume, k_B is the Boltzmann constant, T is the temperature of the chamber and $\frac{dP}{dt}$ is the change in pressure over time which corresponds to the slope of the line in Figure 7.7B. The extracted molecular flow rates through the channel are presented as data points in Figure 7.7C.

As discussed in a previous chapter, some unwanted leaking of gases from the interface between the chip and the holder was unavoidable. This leakrate can be quantified from the data presented in in Figure 7.7C as the flowrate at 0 bar inlet pressure, giving a rate of approximately 10^{11} molecules/s.

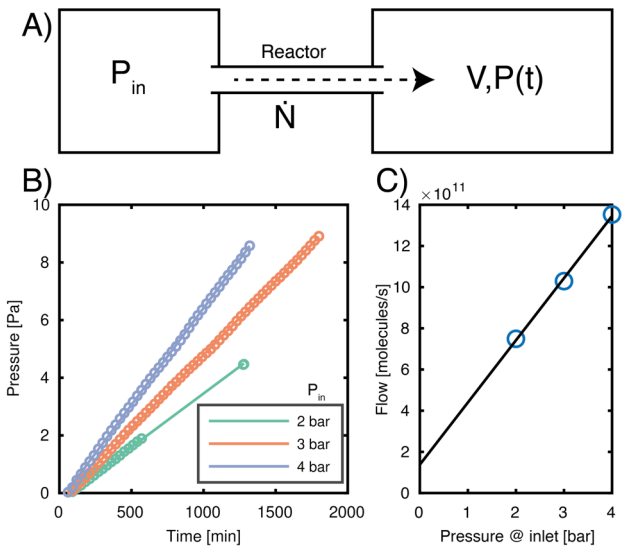

Figure 7.7. **Flow measurement.** A) Schematic representation of the flow measurement where the nanoreactor (center) is connected to a high-pressure side (inlet) and a low-pressure side (outlet) with a closed volume that is gradually filled by the flow through the reactor ($\dot{N}$), resulting in a gradually increasing pressure P(t). B) Pressure in the closed volume vs time for three different applied inlet pressures. C) The calculated molecular flow rates as a function of inlet pressure.

7.2.2 Pressure profile in nanoreactor

An important factor to consider when designing the nanoreactor system was the pressure profile inside the channels. However, due to the nanoscale size of the system, getting real

pressure measurements with a good spatial resolution inside the channels is a non-trivial task. To attain this information, a combination of a numerical flow model and a nanoparticle-based pressure measurement was used. In Figure 7.8 a nanoreactor design is presented (A) with its corresponding simulated pressure profile (B and C), obtained using a rarefied gas flow model valid for the whole Knudsen number regime.[168] From this model the most dramatic pressure drop can be seen to occur over the most narrow part of the channel.

To experimentally address the pressure profile, I make use of the distinct first order phase transition that occurs in polycrystalline Pd nanoparticles as they absorb hydrogen and transform into a hydride, which is also known to affect the LSPR response of the particle.[24] For this experiment, a row of individual Au-Pd hybrid nanoparticles (same structure as Figure 2.7 with Pd as the top material) are placed along the channel, as illustrated in Figure 7.8D by the individually colored dots. By introducing hydrogen gas with a concentration C_{H_2} into the flow of Ar, the position dependent partial pressure of H_2 will be: $P_{H_2}(x) = P(x) \cdot C_{H_2}$, where $P(x)$ is the position dependent pressure in the channel. Furthermore, Pd is known to undergo a first order phase transition to form a hydride when the surrounding partial pressure of H_2 rises above a certain threshold level. At the considered experimental conditions (303 K), this threshold pressure for similar Pd particles is in the range 25-45 mbar. By monitoring the scattering spectra of the nanoparticles while pulses of H_2 are introduced, a clear shift in the full width at half-maximum (FWHM) of the spectrum can be measured as a result of the phase transition. In Figure 7.8E such an experiment, using an inlet pressure of 2 bar, is summarized, where they gray bars indicate pulses of hydrogen with different concentration, using Ar as carrier gas. Simultaneously, the optical response of 21 nanoparticles placed along the nanoreactor is monitored by DFSS.

Looking at the single particle responses it can be seen that most particles undergo a phase transition for 3.5 % and 4 % H_2, except the bottom two. This can be explained by the partial pressure of H_2 never reaching above the required threshold pressure in the lower end of the channel. This is in good agreement with the estimated pressure drop based on the model simulations that predict a partial pressure of H_2 below 32 mbar (at a H_2 concentration of 4 %) in the last 50 μm of the channel (right axis Figure 7.8C), where the two particles are located. As the H_2 concentration is decreased further, most particles along the wider part of the channel respond down to a H_2 concentration of 1.5 %, with some variation due to particle-particle differences.[24] As a general trend, particles placed further downstream require a higher H_2 concentration to induce phase transition, which is especially clear when turning to the particles placed in the narrow part of the channel. This agrees well with the simulated profile that shows a steep pressure gradient along the narrow part of the channel, demonstrating that these Pd nanoparticles can be used as nanoscale pressure sensors to estimate relative pressure profiles inside nanoscale confinements.

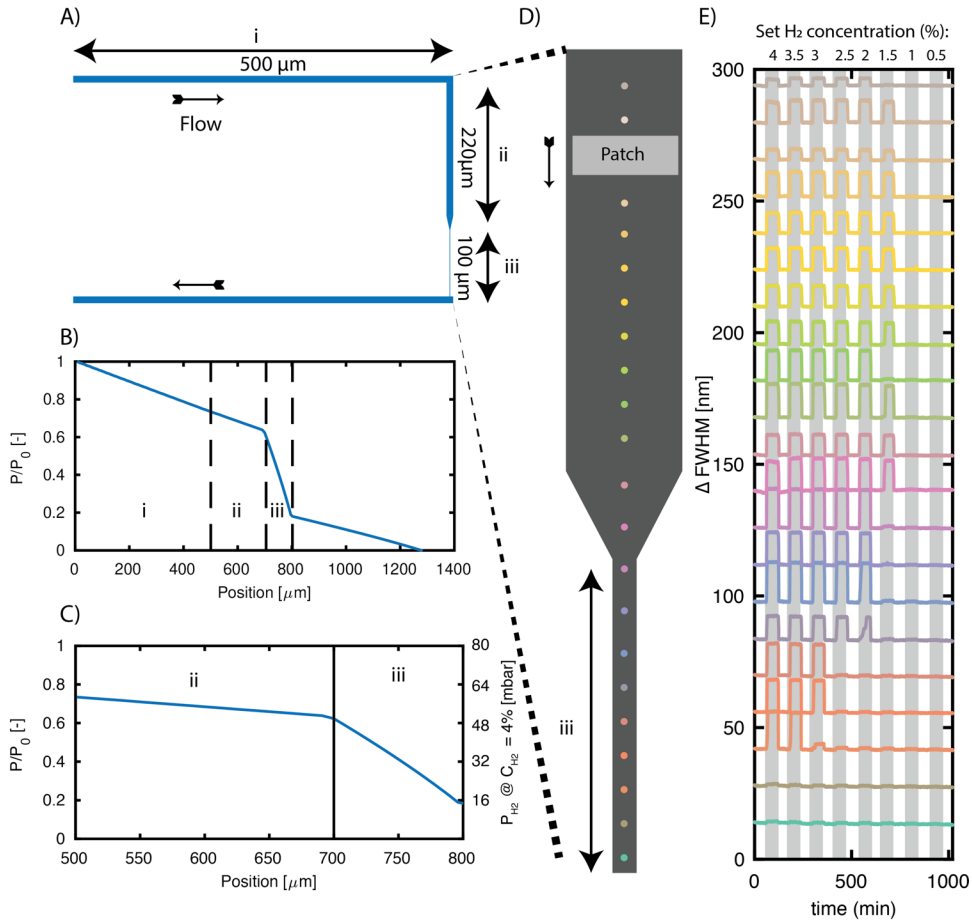

Figure 7.8 **Nanoreactor pressure profile.** A) Nanochannel design used for the simulation and experiment. The depth of the channels is 100 nm and the width is 10 µm at the wider parts down to 900 nm in the narrow channel. B) Simulated relative pressure profile along the channel length with the same regions marked by roman letters as in A). P_0 corresponds to the pressure at the entrance of the channel. C) Zoomed in view of the pressure profile in B) corresponding to the central region of the nanochannel. The right y axis indicates the estimated partial pressure of H_2 with an inlet concentration of 4% H_2. D) Schematic of the straight part of the nanochannel containing nanoparticles indicated by colored dots. The area marked as "Patch" corresponds to a region with densely packed nanoparticles. E) Optical response presented as a change in FWHM of the dark field scattering spectra of 21 individual nanoparticles (color coded as in panel D), when exposed to pulses of hydrogen of different concentration indicated at the top of the figure. The individual responses have been shifted vertically for clarity and the absolute value given for the FWHM is arbitrary.

8 Summary and outlook

The main long-term goal of my project is to investigate individual catalytic nanoparticles under realistic conditions and this thesis summarizes the first years of progress towards this goal.

8.1 Summary of appended papers

In **paper I** the general nanofabrication scheme, as well as the methodology for optical readout of individual plasmonic nanoparticles placed inside nanofluidic channels, are presented together with electrodynamics simulations of the optical response. Specifically, we show that it is possible to place individual metallic nanoparticles inside nanofluidic channels by means of electron beam lithography, and that sequential bonding of a glass lid can establish a hermetic seal. The optical readout from individual metal nanoparticles particles is then made possible by dark field scattering spectroscopy (DFSS). In this way, by monitoring the optical response of individual plasmonic Au nanoparticles inside nanochannels immersed in a liquid, we were able to resolve the dynamics of fluid exchange inside the nanochannels, as well as the binding kinetics of thiol molecules on a single Au nanoparticle.

The use of indirect plasmonic sensing to monitor the solid-state chemical transformation of Cu nanoparticles into their bulk oxide was explored in **Paper II**. Here plasmonic heterodimer nanostructures were fabricated by shrinking hole colloidal lithography (SHCL) that allows for large area patterning of identical complex nanostructures. The heterodimer structures were employed to facilitate drift-free sensing of the Cu oxidation kinetics in challenging conditions such as temperature ramps up to 250°C. By combining the obtained optical readout from the heterodimer nanostructures with FDTD simulations, a reaction mechanism could be derived and the dependence of the apparent activation energy on the oxidation fraction of the nanoparticles could be unraveled.

In **Paper III** we present the nanoreactor concept for single particle catalysis in the gas phase and describe in detail both the developed nanoreactor chip and the whole experimental setup constructed around it. We then demonstrate the possibility to use the nanoreactor setup to measure catalyst activity by means of mass spectrometry, and at the same time address individual catalytic nanoparticles under *operando* conditions using plasmonic nanospectroscopy. This makes it possible to correlate structural and/or chemical changes of the catalyst nanoparticles with changes in reactivity at the single particle level. Specifically, CO oxidation over Cu and Pt catalyst nanoparticles was studied and we could show that, in both cases, optically measurable changes of individual particles could be assigned to significant changes in reactivity. Additionally, due to the small reactor dimension attainable using nanofluidics, we could visualize the impact of local reactant consumption at the individual particle level. This opens the door to using nanoreactors as “model pores” to scrutinize the impact of spatial and temporal variations in reactant concentration that occur at the nanoscale.

8.2 Outlook

This thesis presents the development of a new platform for catalyst research and there are several possible ways to continue this work over the coming years. To start with, it would be interesting to try to further optimize the reactor geometry in ways that make detection of reaction products from even smaller sample sizes than the presented ca. 30 000 particles possible. The goal of this would be to make it possible to study *all* the active catalyst particles optically, on an individual level, while measuring their catalytic activity. Another improvement would be to make it possible to study smaller catalytic particles that better resemble real nanoparticles used in heterogeneous catalysis (<5nm). To be able to do this using plasmonic sensing, one could for example make use of better sensing arrangements based on tailored nanoplasmonic structures with strong field enhancements onto which the catalyst particle can be attached. Furthermore, one major limitation of the nanoreactor, at the time being, is that there is no way to open it for *post-mortem* characterization of the particles inside. In this context, it would be a big improvement to design the nanoreactor chip in a way that made it accessible to e.g. an electron beam. This would open up the possibility to do *ex-situ* SEM/TEM analysis of the particles to get information about particle morphology at the different stages of the reaction. One way of achieving this could be to include an etched, electron transparent window in the chip, similar to the in-situ TEM chips that exist already.[103] With this added ability it would be possible to identify unique structural properties of the individual particles that could then be used to explain particle differences under reaction conditions. So far we have only addressed nanoparticles made by evaporation-based techniques. These particles are well defined when it comes to size and shape in 2D but evaporation techniques lack control over crystallinity and 3D structure of the particles. It would therefore be interesting to incorporate chemically synthesized colloidal nanoparticles into the nanoreactors for catalyst testing. Placing of individual nanoparticles from colloidal solutions could be achieved by e.g surface modification inside the channels or by using novel patterning[169] or printing techniques.[170]

Besides studies of catalyst nanoparticles, the nanofluidic platform we have built might be of interest to study fluidics on the nanoscale. For example by expanding on the nanoscale pressure sensor concept discussed in chapter 7 and paper III, pressure measurements with high spatial resolution could be made inside extremely confined geometries. This could potentially be used to verify and improve existing fluid dynamic models.

9 Acknowledgements

I acknowledge financial support from the ERC StG SINCAT and the Knut and Alice Wallenberg Foundation project 2015.0055, and thank the Knut and Alice Wallenberg Foundation for their support of the infrastructure in the MC2 nanofabrication laboratory at Chalmers.

There are also a lot of people that have helped me along the way and although I cannot mention everyone, here are some people I want to acknowledge.

First of all, thanks to my main supervisor Christoph for giving me the opportunity to join this adventure! Your passion, encouragement and positivity is something I really appreciate.

Thanks also to my co-supervisor Hanna Härelind.

Thanks to my examiner Henrik Grönbeck for the feedback on this thesis and for taking care of the Chemical Physics division.

A big thanks to Stephan for designing and building everything surrounding the nanoreactor chip as well as for good times both in and outside Chalmers.

Thanks to Joachim for teaching me more or less everything I know about nanofabrication. Keep the new (crazy?) ideas coming and good luck with the future house!

All the past and present members of the Langhammer group, it's a really nice group to be a part of! An extra thanks to my office mate Ferry for great discussions and inspiration, your dedication and ability to get things done is really impressive.

Thanks to Sara for our collaborations and for the nice conference trips. 

Thanks to all collaborators on different projects with a special thanks to Tomasz for teaching me FDTD and to Henrik Ström for the flow simulations as well as a nice Bremen trip.

I'm also grateful to everyone at Chemical Physics, it's really nice to always have great company for lunches and fika. Among you, a special thanks to Mikkel for nice discussions including everything from salmon to catalysis and even combinations of the two.

Thanks to everyone involved in the KAW project for inspiring collaborations and discussions.

Finally, a big thanks to my friends and family with a special thanks to Matilda for making my life outside of Chalmers great!

Bibliography

1. Eigler, D. M. & Schweizer, E. K. Positioning single atoms with a scanning tunnelling microscope. *Nature* **344,** 524–526 (1990).

2. Lu, W. & Lieber, C. M. Nanoelectronics from the bottom up. *Nat. Mater.* **6,** 841–850 (2007).

3. Agasti, S. S. *et al.* Nanoparticles for detection and diagnosis. *Adv. Drug Deliv. Rev.* **62,** 316–328 (2010).

4. Bell, A. T. The impact of nanoscience on heterogeneous catalysis. *Science* **299,** 1688–91 (2003).

5. Barber, D. J. & Frestone, I. C. An Investigation of the origin of the colour of the Lycurgus cup by analytical transmission electron microscopy. *Archaeometry* **32,** 33–45 (1990).

6. Dyck, O., Kim, S., Kalinin, S. V. & Jesse, S. Placing single atoms in graphene with a scanning transmission electron microscope. *Appl. Phys. Lett.* **111,** 113104 (2017).

7. Chorkendorff, I. & Niemantsverdriet, J. W. *Concepts of modern catalysis and kinetics*. (Wiley-VCH, 2007).

8. Ertl, G. Reactions at surfaces: From atoms to complexity (nobel lecture). *Angewandte Chemie - International Edition* **47,** 3524–3535 (2008).

9. Unger, K. K. *Characterization of porous solids : proceedings of the IUPAC symposium (COPS I), Bad Soden a. Ts., F.R.G., April 26-29, 1987*. (Elsevier, 1988).

10. Karsl, O. & Bluhm, H. *Operando Research in Heterogeneous Catalysis*. **114,** (Springer International Publishing, 2017).

11. Kooyman, P. J. Development of Operando transmission electron microscopy. in *Springer Series in Chemical Physics* **114,** 111–129 (2017).

12. van Spronsen, M. A., van Baarle, G. J. C., Herbschleb, C. T., Frenken, J. W. M. & Groot, I. M. N. High-pressure operando STM studies giving insight in CO oxidation and NO reduction over Pt(1 1 0). *Catal. Today* **244,** 85–95 (2015).

13. Zhao, S. *et al.* Operando Characterization of Catalysts through use of a Portable Microreactor. *ChemCatChem* **7,** 3683–3691 (2015).

14. Rodríguez, J. A. *et al. In-situ Characterization of Heterogeneous Catalysts*. (John Wiley & Sons, Inc., 2013). doi:10.1002/9781118355923

15. Sambur, J. B. & Chen, P. Approaches to Single-Nanoparticle Catalysis. *Annu. Rev. Phys. Chem.* **65,** 395–422 (2014).

16. Bocquet, L. & Charlaix, E. Nanofluidics, from bulk to interfaces. *Chem. Soc. Rev.* **39,** 1073–1095 (2010).

17. Eijkel, J. C. T. & Berg, A. van den. Nanofluidics: what is it and what can we expect from it? *Microfluid. Nanofluidics* **1,** 249–267 (2005).

18. Cao, B.-Y., Sun, J., Chen, M. & Guo, Z.-Y. Molecular Momentum Transport at Fluid-Solid Interfaces in MEMS/NEMS: A Review. *Int. J. Mol. Sci.* **10,** 4638–4706 (2009).

19. Larsson, E. M., Syrenova, S., Langhammer, C. & Giessen, H. Nanoplasmonic sensing for nanomaterials science. *Nanophotonics* **1,** 249–266 (2012).

20. Taylor, A. B. & Zijlstra, P. Single-Molecule Plasmon Sensing: Current Status and Future Prospects. *ACS Sensors* **2,** 1103–1122 (2017).

21. Anker, J. N. *et al.* Biosensing with plasmonic nanosensors. *Nat. Mater.* **7,** 442–453 (2008).

22. Larsson, E. M., Langhammer, C., Zoric, I. & Kasemo, B. Nanoplasmonic Probes of Catalytic Reactions. *Science (80-.).* **326,** 1091–1094 (2009).

23. Syrenova, S. *et al.* Hydride formation thermodynamics and hysteresis in individual Pd nanocrystals with different size and shape. *Nat Mater* **14,** 1236–1244 (2015).

24. Alekseeva, S. *et al.* Grain boundary mediated hydriding phase transformations in individual polycrystalline metal nanoparticles. *Nat. Commun.* **8,** 1084 (2017).

25. Liu, N., Tang, M. L., Hentschel, M., Giessen, H. & Alivisatos, A. P. Nanoantenna-enhanced gas sensing in a single tailored nanofocus. *Nat. Mater.* **10,** 631–636 (2011).

26. Museum, T. B. Lycurgus Cup. Available at: http://www.britishmuseum.org/research/collection_online/collection_object_details/collection_image_gallery.aspx?assetId=36154001&objectId=61219&partId=1#more-views. (Accessed: 6th August 2018)

27. Kelly, K. L., Coronado, E., Zhao, L. L. & Schatz, G. C. The optical properties of metal nanoparticles: The influence of size, shape, and dielectric environment. *J. Phys. Chem. B* **107,** 668–677 (2003).

28. Novo, C., Funston, A. M. & Mulvaney, P. Direct observation of chemical reactions on single gold nanocrystals using surface plasmon spectroscopy. *Nat. Nanotechnol.* **3,** 598–602 (2008).

29. Langhammer, C. & Larsson, E. M. Nanoplasmonic In Situ Spectroscopy for Catalysis Applications. *ACS Catal.* **2,** 2036–2045 (2012).

30. Tittl, A., Giessen, H. & Liu, N. Plasmonic gas and chemical sensing. in *Nanomaterials and Nanoarchitectures: A Complex Review of Current Hot Topics and their Applications* 239–272 (2015). doi:10.1007/978-94-017-9921-8_8

31. Langhammer, C., Zorić, I., Kasemo, B. & Clemens, B. M. Hydrogen storage in Pd nanodisks characterized with a novel nanoplasmonic sensing scheme. *Nano Lett.* **7,** 3122–3127 (2007).

32. Mie, G. Beiträge zur Optik trüber Medien, speziell kolloidaler Metallösungen. *Ann. Phys.* **330,** 377–445 (1908).

33. Maier, S. A. *Plasmonics: Fundamentals and applications*. (Springer US, 2007). doi:10.1007/0-387-37825-1

34. Schwind, M. *et al.* Nanoplasmonic Sensing for Monitoring the Initial Stages of Atmospheric Corrosion of Cu Nanodisks and Thin Films. *J. Electrochem. Soc.* **160,** C487–C492 (2013).

35. Pirzadeh, Z., Pakizeh, T., Miljkovic, V., Langhammer, C. & Dmitriev, A. Plasmon–Interband Coupling in Nickel Nanoantennas. *ACS Photonics* **1,** 158–162 (2014).

36. Langhammer, C., Schwind, M., Kasemo, B. & Zorić, I. Localized Surface Plasmon Resonances in Aluminum Nanodisks. *Nano Lett.* **8,** 1461–1471 (2008).

37. Langhammer, C., Yuan, Z., Zorić, I. & Kasemo, B. Plasmonic Properties of Supported Pt and Pd Nanostructures. *Nano Lett.* **6,** 833–838 (2006).

38. Bansal, A. & Verma, S. S. Optical response of noble metal alloy nanostructures. *Phys. Lett. A* **379,** 163–169 (2015).

39. Nugroho, F. A. A., Iandolo, B., Wagner, J. B. & Langhammer, C. Bottom-Up Nanofabrication of Supported Noble Metal Alloy Nanoparticle Arrays for Plasmonics. *ACS Nano* **10,** 2871–2879 (2016).

40. Lalisse, A., Tessier, G., Plain, J. & Baffou, G. Plasmonic efficiencies of nanoparticles made of metal nitrides (TiN, ZrN) compared with gold. *Sci. Rep.* **6,** 38647 (2016).

41. Wokaun, A., Gordon, J. P. & Liao, P. F. Radiation Damping in Surface-Enhanced Raman Scattering. *Phys. Rev. Lett.* **48,** 957–960 (1982).

42. Zhao, J. *et al.* Methods for Describing the Electromagnetic Properties of Silver and Gold Nanoparticles. *Acc. Chem. Res.* **41,** 1710–1720 (2008).

43. Taflove, A., Hagness, S. C. & Piket-May, M. Computational Electromagnetics: The Finite-Difference Time-Domain Method. in *The Electrical Engineering Handbook* 629–670 (Elsevier, 2005). doi:10.1016/B978-012170960-0/50046-3

44. García de Abajo, F. J. & Howie, A. Retarded field calculation of electron energy loss in inhomogeneous dielectrics. *Phys. Rev. B* **65,** 115418 (2002).

45. Rechberger, W. *et al.* Optical properties of two interacting gold nanoparticles. *Opt. Commun.* **220,** 137–141 (2003).

46. Sheikholeslami, S., Jun, Y. W., Jain, P. K. & Alivisatos, A. P. Coupling of optical resonances in a compositionally asymmetric plasmonic nanoparticle dimer. *Nano Lett.* **10,** 2655–2660 (2010).

47. Nordlander, P., Oubre, C., Prodan, E., Li, K. & Stockman, M. I. Plasmon hybridization in nanoparticle dimers. *Nano Lett.* **4,** 899–903 (2004).

48. Prodan, E., Radloff, C., Halas, N. J. & Nordlander, P. A hybridization model for

the plasmon response of complex nanostructures. *Science* **302,** 419–22 (2003).

49. Flauraud, V. *et al.* Mode Coupling in Plasmonic Heterodimers Probed with Electron Energy Loss Spectroscopy. *ACS Nano* **11,** 3485–3495 (2017).

50. Zorić, I., Zäch, M., Kasemo, B. & Langhammer, C. Gold, Platinum, and Aluminum Nanodisk Plasmons: Material Independence, Subradiance, and Damping Mechanisms. *ACS Nano* **5,** 2535–2546 (2011).

51. Jensen, T. R., Malinsky, M. D., Haynes, C. L. & Van Duyne, R. P. Nanosphere Lithography: Tunable Localized Surface Plasmon Resonance Spectra of Silver Nanoparticles. *J. Phys. Chem. B* **104,** 10549–10556 (2000).

52. Traci R. Jensen *et al.* Nanosphere Lithography: Effect of the External Dielectric Medium on the Surface Plasmon Resonance Spectrum of a Periodic Array of Silver Nanoparticles. (1999). doi:10.1021/JP9926802

53. Englebienne, P. Use of colloidal gold surface plasmon resonance peak shift to infer affinity constants from the interactions between protein antigens and antibodies specific for single or multiple epitopes. *Analyst* **123,** 1599–1603 (1998).

54. Foerster, B., Rutten, J., Pham, H., Link, S. & Sönnichsen, C. Particle Plasmons as Dipole Antennas: State Representation of Relative Observables. *J. Phys. Chem. C* acs.jpcc.8b06350 (2018). doi:10.1021/acs.jpcc.8b06350

55. Dahlin, A. B., Tegenfeldt, J. O. & Höök, F. Improving the instrumental resolution of sensors based on localized surface plasmon resonance. *Anal. Chem.* **78,** 4416–4423 (2006).

56. Jackman, J. A., Rahim Ferhan, A. & Cho, N. J. Nanoplasmonic sensors for biointerfacial science. *Chemical Society Reviews* **46,** 3615–3660 (2017).

57. Haes, A. J., Zou, S., Schatz, G. C. & Van Duyne, R. P. Nanoscale optical biosensor: Short range distance dependence of the localized surface plasmon resonance of noble metal nanoparticles. *J. Phys. Chem. B* **108,** 6961–6968 (2004).

58. Wadell, C. & Langhammer, C. Drift-corrected nanoplasmonic hydrogen sensing by polarization. *Nanoscale* **7,** 10963–10969 (2015).

59. Wadell, C., Syrenova, S. & Langhammer, C. Plasmonic hydrogen sensing with nanostructured metal hydrides. *ACS Nano* **8,** 11925–11940 (2014).

60. Syrenova, S. *Nanoplasmonic Spectroscopy of Single Nanoparticles Tracking Size and Shape Effects in Pd Hydride Formation*. (Institutionen för teknisk fysik, Kemisk fysik, Chalmers tekniska högskola, 2014).

61. Langhammer, C., Zhdanov, V. P., Zorić, I. & Kasemo, B. Size-dependent kinetics of hydriding and dehydriding of Pd nanoparticles. *Phys. Rev. Lett.* **104,** (2010).

62. Shegai, T. & Langhammer, C. Hydride formation in single palladium and magnesium nanoparticles studied by nanoplasmonic dark-field scattering spectroscopy. *Adv. Mater.* **23,** 4409–4414 (2011).

63. Duan, X., Kamin, S., Sterl, F., Giessen, H. & Liu, N. Hydrogen-Regulated Chiral Nanoplasmonics. *Nano Lett.* **16,** 1462–1466 (2016).

64. Sterl, F. *et al.* Nanoscale Hydrogenography on Single Magnesium Nanoparticles. *Nano Lett.* acs.nanolett.8b01277 (2018). doi:10.1021/acs.nanolett.8b01277

65. Rice, K. P., Walker, E. J., Stoykovich, M. P. & Saunders, A. E. Solvent-dependent surface plasmon response and oxidation of copper nanocrystals. *J. Phys. Chem. C* **115,** 1793–1799 (2011).

66. Susman, M. D., Feldman, Y., Bendikov, T. A., Vaskevich, A. & Rubinstein, I. Real-time plasmon spectroscopy study of the solid-state oxidation and Kirkendall void formation in copper nanoparticles. *Nanoscale* **9,** 12573–12589 (2017).

67. Mayer, K. M. & Hafner, J. H. Localized surface plasmon resonance sensors. *Chem. Rev.* **111,** 3828–3857 (2011).

68. Langhammer, C., Larsson, E. M., Kasemo, B. & Zorić, I. Indirect Nanoplasmonic Sensing: Ultrasensitive Experimental Platform for Nanomaterials Science and Optical Nanocalorimetry. *Nano Lett.* **10,** 3529–3538 (2010).

69. Larsson, E. M. *et al.* Real Time Indirect Nanoplasmonic in Situ Spectroscopy of Catalyst Nanoparticle Sintering. *ACS Catal.* **2,** 238–245 (2012).

70. Ringe, E., Sharma, B., Henry, A.-I., Marks, L. D. & Van Duyne, R. P. Single nanoparticle plasmonics. *Phys. Chem. Chem. Phys. Phys. Chem. Chem. Phys. Phys. Chem. Chem. Phys* **1515121,** 4075–4460 (2013).

71. Ohtsu, M. *Progress in Nanophotonics 1*. (Springer Berlin Heidelberg, 2011). doi:10.1007/978-3-642-17481-0

72. Tanaka, Y. *et al.* Direct imaging of nanogap-mode plasmon-resonant fields. *Opt. Express* **19,** 7726–7733 (2011).

73. Imura, K., Nagahara, T. & Okamoto, H. Near-field optical imaging of plasmon modes in gold nanorods. *J. Chem. Phys.* **122,** 154701 (2005).

74. Cinchetti, M. *et al.* Photoemission Electron Microscopy as a Tool for the Investigation of Optical Near Fields. *Phys. Rev. Lett.* **95,** 047601 (2005).

75. Sun, Q. *et al.* Direct imaging of the near field and dynamics of surface plasmon resonance on gold nanostructures using photoemission electron microscopy. *Light Sci. Appl.* **2,** e118–e118 (2013).

76. Chaturvedi, P. *et al.* Imaging of Plasmonic Modes of Silver Nanoparticles Using High-Resolution Cathodoluminescence Spectroscopy. *ACS Nano* **3,** 2965–2974 (2009).

77. García de Abajo, F. J. & Kociak, M. Probing the Photonic Local Density of States with Electron Energy Loss Spectroscopy. *Phys. Rev. Lett.* **100,** 106804 (2008).

78. Boyer, D., Tamarat, P., Maali, A., Lounis, B. & Orrit, M. Photothermal imaging of nanometer-sized metal particles among scatterers. *Science* **297,** 1160–3 (2002).

79. Pini, V. *et al.* Spatially multiplexed dark-field microspectrophotometry for

nanoplasmonics. *Sci. Rep.* **6,** 22836 (2016).

80. Zopf, D. *et al.* Hyperspectral imaging of plasmon resonances in metallic nanoparticles. *Biosens. Bioelectron.* **81,** 287–293 (2016).

81. Berzelius, J. J. Årsberättelsen om framsteg i fysik och kemi. (1835).

82. Ostwald, W. Catalysis. *Phys. Zeitschrift* **3,** 313–322 (1901).

83. Appl, M. & Wiley InterScience (Online service). *Ammonia : principles and industrial practice*. (Wiley-VCH, 1999).

84. Haber, F. & Koenig, A. Wissenschaftliche Übersichten: Oxydation des Luftstickstoffes. *Zeitschrift für Elektrotechnik und Elektrochemie* **16,** 11–25 (1910).

85. Haber, F. & Rossignol, R. Le. Über die technische Darstellung von Ammoniak aus den Elementen. *Zeitschrift für Elektrochemie und Angew. Phys. Chemie* **19,** 53–72 (1913).

86. Papp, C. From Flat Surfaces to Nanoparticles: In Situ Studies of the Reactivity of Model Catalysts. *Catal. Letters* **147,** 2–19 (2017).

87. Jørgensen, M. & Grönbeck, H. Scaling Relations and Kinetic Monte Carlo Simulations To Bridge the Materials Gap in Heterogeneous Catalysis. *ACS Catal.* **7,** 5054–5061 (2017).

88. Persson, H., Thormählen, P., Zhdanov, V. P. & Kasemo, B. Monte Carlo simulations of the kinetics of catalytic reactions on nanometer-sized particles, with diffusion over facet boundaries. *J. Vac. Sci. Technol. A Vacuum, Surfaces, Film.* **17,** 1721 (1999).

89. Narayan, T. C. *et al.* Direct visualization of hydrogen absorption dynamics in individual palladium nanoparticles. *Nat. Commun.* **8,** 14020 (2017).

90. Narayan, T. C., Baldi, A., Koh, A. L., Sinclair, R. & Dionne, J. A. Reconstructing solute-induced phase transformations within individual nanocrystals. *Nat. Mater.* **15,** 768–774 (2016).

91. Baldi, A., Narayan, T. C., Koh, A. L. & Dionne, J. A. In situ detection of hydrogen-induced phase transitions in individual palladium nanocrystals. *Nat. Mater.* **13,** 1143–1148 (2014).

92. Thomas, J. M. (John M. & Thomas, W. J. *Principles and practice of heterogeneous catalysis*.

93. Stoltze, P. & Nørskov, J. K. Bridging the 'pressure gap' between ultrahigh-vacuum surface physics and high-pressure catalysis. *Phys. Rev. Lett.* **55,** 2502–2505 (1985).

94. Gustafson, J. *et al.* The Role of Oxides in Catalytic CO Oxidation over Rhodium and Palladium. *ACS Catal.* **8,** 4438–4445 (2018).

95. van Spronsen, M. A., Frenken, J. W. M. & Groot, I. M. N. Surface science under reaction conditions: CO oxidation on Pt and Pd model catalysts. *Chem. Soc. Rev.*

46, 4347–4374 (2017).

96. Chakrabarti, A. *et al.* A decade+ of operando spectroscopy studies. *Catal. Today* **283,** 27–53 (2017).

97. Herbschleb, C. T. *et al.* The ReactorSTM: Atomically resolved scanning tunneling microscopy under high-pressure, high-temperature catalytic reaction conditions. *Rev. Sci. Instrum.* **85,** 083703 (2014).

98. Roobol, S. B. *et al.* The ReactorAFM : Non-contact atomic force microscope operating under high-pressure and high-temperature catalytic conditions. *Rev. Sci. Instrum.* **86,** 033706 (2015).

99. Knudsen, J., Andersen, J. N. & Schnadt, J. A versatile instrument for ambient pressure x-ray photoelectron spectroscopy: The Lund cell approach. *Surf. Sci.* **646,** 160–169 (2016).

100. Hansen, P. L. *et al.* Atom-resolved imaging of dynamic shape changes in supported copper nanocrystals. *Science* **295,** 2053–5 (2002).

101. van Schrojenstein Lantman, E. M., Deckert-Gaudig, T., Mank, A. J. G., Deckert, V. & Weckhuysen, B. M. Catalytic processes monitored at the nanoscale with tip-enhanced Raman spectroscopy. *Nat. Nanotechnol.* **7,** 583–586 (2012).

102. de Smit, E. *et al.* Nanoscale chemical imaging of a working catalyst by scanning transmission X-ray microscopy. *Nature* **456,** 222–225 (2008).

103. Vendelbo, S. B. *et al.* Visualization of oscillatory behaviour of Pt nanoparticles catalysing CO oxidation. *Nat. Mater.* **13,** 884–890 (2014).

104. Kohn, W. & Sham, L. J. Self-Consistent Equations Including Exchange and Correlation Effects. *Phys. Rev.* **140,** A1133–A1138 (1965).

105. Jones, R. O. Density functional theory: Its origins, rise to prominence, and future. *Rev. Mod. Phys.* **87,** 897–923 (2015).

106. Jinnouchi, R. & Asahi, R. Predicting Catalytic Activity of Nanoparticles by a DFT-Aided Machine-Learning Algorithm. *J. Phys. Chem. Lett.* **8,** 4279–4283 (2017).

107. Renken, A. & Kiwi-Minsker, L. Microstructured Catalytic Reactors. *Adv. Catal.* **53,** 47–122 (2010).

108. Tanimu, A., Jaenicke, S. & Alhooshani, K. Heterogeneous catalysis in continuous flow microreactors: A review of methods and applications. *Chem. Eng. J.* **327,** 792–821 (2017).

109. Yue, J., Schouten, J. C. & Nijhuis, T. A. Integration of Microreactors with Spectroscopic Detection for Online Reaction Monitoring and Catalyst Characterization. *Ind. Eng. Chem. Res.* **51,** 14583–14609 (2012).

110. Bu, Y., Niemantsverdriet, J. W. H. & Fredriksson, H. O. A. Cu Model Catalyst Dynamics and CO Oxidation Kinetics Studied by Simultaneous in Situ UV-Vis and Mass Spectroscopy. *ACS Catal.* **6,** 2867–2876 (2016).

111. Kiwi-Minsker, L. & Renken, A. Microstructured reactors for catalytic reactions. *Catal. Today* **110,** 2–14 (2005).

112. Rebrov, E. V. Heterogeneous Catalysis in Microreactors. in *Microreactors in Preparative Chemistry* 243–271 (Wiley-VCH Verlag GmbH & Co. KGaA, 2013). doi:10.1002/9783527652891.ch10

113. Wiles, C. & Watts, P. Continuous process technology: a tool for sustainable production. *Green Chem.* **16,** 55–62 (2014).

114. Jähnisch, K., Hessel, V., Löwe, H. & Baerns, M. Chemistry in Microstructured Reactors. *Angew. Chemie Int. Ed.* **43,** 406–446 (2004).

115. Henriksen, T. R., Olsen, J. L., Vesborg, P., Chorkendorff, I. & Hansen, O. Highly sensitive silicon microreactor for catalyst testing. *Rev. Sci. Instrum.* **80,** 124101 (2009).

116. Vesborg, P. C. K., Olsen, J. L., Henriksen, T. R., Chorkendorff, I. & Hansen, O. Gas-phase photocatalysis in µ-reactors. *Chem. Eng. J.* **160,** 738–741 (2010).

117. Dionigi, F. *et al.* A transparent Pyrex µ-reactor for combined *in situ* optical characterization and photocatalytic reactivity measurements. *Rev. Sci. Instrum.* **84,** 103910 (2013).

118. Kehres, J. *et al.* Novel micro-reactor flow cell for investigation of model catalysts using *in situ* grazing-incidence X-ray scattering. *J. Synchrotron Radiat.* **23,** 455–463 (2016).

119. Baier, S., Rochet, A., Hofmann, G., Kraut, M. & Grunwaldt, J.-D. Lithographically fabricated silicon microreactor for in situ characterization of heterogeneous catalysts—Enabling correlative characterization techniques. *Rev. Sci. Instrum.* **86,** 065101 (2015).

120. Cao, E., Firth, S., McMillan, P. F. & Gavriilidis, A. Application of microfabricated reactors for operando Raman studies of catalytic oxidation of methanol to formaldehyde on silver. *Catal. Today* **126,** 119–126 (2007).

121. Beale, A. M., van der Eerden, A. M. J., Kervinen, K., Newton, M. A. & Weckhuysen, B. M. Adding a third dimension to operando spectroscopy: a combined UV-Vis, Raman and XAFS setup to study heterogeneous catalysts under working conditions. *Chem. Commun.* **0,** 3015 (2005).

122. Tan, C. K. C., Delgass, W. N. & Baertsch, C. D. Spatially resolved in situ FTIR analysis of CO adsorption and reaction on Pt/SiO2 in a silicon microreactor. *Appl. Catal. B Environ.* **93,** 66–74 (2009).

123. Creemer, J. F. *et al.* Atomic-scale electron microscopy at ambient pressure. *Ultramicroscopy* **108,** 993–998 (2008).

124. Xin, H. L., Niu, K., Alsem, D. H. & Zheng, H. In Situ TEM Study of Catalytic Nanoparticle Reactions in Atmospheric Pressure Gas Environment. *Microsc. Microanal.* **19,** 1558–1568 (2013).

125. Ertl, G. Reactions at well-defined surfaces. *Surf. Sci.* **299–300,** 742–754 (1994).

126. Zambelli, T., Barth, J. V., Wintterlin, J. & Ertl, G. Complex pathways in dissociative adsorption of oxygen on platinum. *Nature* **390,** 495–497 (1997).

127. Burnett, D. J. *et al.* In-situ soft X-ray studies of CO oxidation on the Pt(1 1 1) surface. *Surf. Sci.* **564,** 29–37 (2004).

128. Zhdanov, V. P. & Kasemo, B. Kinetic phase transitions in simple reactions on solid surfaces. *Surf. Sci. Rep.* **20,** 113–189 (1994).

129. Imbihl, R. & Ertl, G. Oscillatory Kinetics in Heterogeneous Catalysis. *Chem. Rev.* **95,** 697–733 (1995).

130. Hendriksen, B. L. M. & Frenken, J. W. M. CO Oxidation on Pt(110): Scanning Tunneling Microscopy Inside a High-Pressure Flow Reactor. *Phys. Rev. Lett.* **89,** 046101 (2002).

131. Xu, Y. Nanofluidics: A New Arena for Materials Science. *Adv. Mater.* **30,** 1702419 (2018).

132. Mawatari, K., Kazoe, Y., Shimizu, H., Pihosh, Y. & Kitamori, T. Extended-Nanofluidics: Fundamental Technologies, Unique Liquid Properties, and Application in Chemical and Bio Analysis Methods and Devices. *Anal. Chem.* **86,** 4068–4077 (2014).

133. Kim, S. J., Wang, Y.-C., Lee, J. H., Jang, H. & Han, J. Concentration Polarization and Nonlinear Electrokinetic Flow near a Nanofluidic Channel. *Phys. Rev. Lett.* **99,** 044501 (2007).

134. Louër, A.-C. *et al.* Pressure-Assisted Selective Preconcentration in a Straight Nanochannel. *Anal. Chem.* **85,** 7948–7956 (2013).

135. Gamble, T. *et al.* Rectification of Ion Current in Nanopores Depends on the Type of Monovalent Cations: Experiments and Modeling. *J. Phys. Chem. C* **118,** 9809–9819 (2014).

136. Zhang, M. *et al.* Light and pH Cooperative Nanofluidic Diode Using a Spiropyran-Functionalized Single Nanochannel. *Adv. Mater.* **24,** 2424–2428 (2012).

137. Xu, Y. & Xu, B. An Integrated Glass Nanofluidic Device Enabling In-situ Electrokinetic Probing of Water Confined in a Single Nanochannel under Pressure-Driven Flow Conditions. *Small* **11,** 6165–6171 (2015).

138. Hibara, A. *et al.* Nanochannels on a Fused-Silica Microchip and Liquid Properties Investigation by Time-Resolved Fluorescence Measurements. *Anal. Chem.* **74,** 6170–6176 (2002).

139. Tas, N. R., Haneveld, J., Jansen, H. V., Elwenspoek, M. & van den Berg, A. Capillary filling speed of water in nanochannels. *Appl. Phys. Lett.* **85,** 3274–3276 (2004).

140. Bocquet, L. & Tabeling, P. Physics and technological aspects of nanofluidics. *Lab Chip* **14,** 3143–3158 (2014).

141. Haywood, D. G., Saha-Shah, A., Baker, L. A. & Jacobson, S. C. Fundamental Studies of Nanofluidics: Nanopores, Nanochannels, and Nanopipets. *Anal. Chem.* **87,** 172–187 (2015).

142. Sparreboom, W., van den Berg, A. & Eijkel, J. C. T. Principles and applications of nanofluidic transport. *Nat. Nanotechnol.* **4,** 713–720 (2009).

143. Viefhues, M., Regtmeier, J. & Anselmetti, D. Fast and continuous-flow separation of DNA-complexes and topological DNA variants in microfluidic chip format. *Analyst* **138,** 186–196 (2013).

144. Regtmeier, J., Käsewieter, J., Everwand, M. & Anselmetti, D. Continuous-flow separation of nanoparticles by electrostatic sieving at a micro-nanofluidic interface. *J. Sep. Sci.* **34,** 1180–1183 (2011).

145. Tegenfeldt, J. O. *et al.* The dynamics of genomic-length DNA molecules in 100-nm channels. *Proc. Natl. Acad. Sci.* **101,** 10979–10983 (2004).

146. Müller, V. & Westerlund, F. Optical DNA mapping in nanofluidic devices: principles and applications. *Lab Chip* **17,** 579–590 (2017).

147. Prakash, S. & Yeom, J. *Nanofluidics and Microfluidics*. (Elsevier, 2014). doi:10.1016/C2010-0-66159-1

148. Xu, Y., Matsumoto, N., Wu, Q., Shimatani, Y. & Kawata, H. Site-specific nanopatterning of functional metallic and molecular arbitrary features in nanofluidic channels. *Lab Chip* **15,** 1989–1993 (2015).

149. Chen, Y. Nanofabrication by electron beam lithography and its applications: A review. *Microelectron. Eng.* **135,** 57–72 (2015).

150. Tseng, A. A. (Ampere A. . *Nanofabrication : fundamentals and applications*. (World Scientific, 2008).

151. Stepanova, M. & Dew, S. *Nanofabrication*. *Techniques and Principles* **9783709104,** (Springer Vienna, 2012).

152. Williams, K. R., Gupta, K. & Wasilik, M. Etch rates for micromachining processing-part II. *J. Microelectromechanical Syst.* **12,** 761–778 (2003).

153. Laermer, F. & Schilp, A. Method of anisotropically etching silicon. (1996).

154. Deal, B. E. & Grove, A. S. General Relationship for the Thermal Oxidation of Silicon. *J. Appl. Phys.* **36,** 3770–3778 (1965).

155. BYU Electrical and computer engineering. Oxide Thickness Calculator | BYU Cleanroom. Available at: http://cleanroom.byu.edu/OxideThickCalc. (Accessed: 28th May 2018)

156. Ohring, M. *Materials Science of Thin Films*. *Materials Science* **29,** (Elsevier, 2002).

157. Yang, S.-M., Jang, S. G., Choi, D.-G., Kim, S. & Yu, H. K. Nanomachining by Colloidal Lithography. *Small* **2,** 458–475 (2006).

158. Fredriksson, H. *et al.* Hole-mask colloidal lithography. *Adv. Mater.* **19,** 4297–4302 (2007).

159. Hanarp, P., Sutherland, D. S., Gold, J. & Kasemo, B. Control of nanoparticle film structure for colloidal lithography. *Colloids Surfaces A Physicochem. Eng. Asp.* **214,** 23–36 (2003).

160. Syrenova, S., Wadell, C. & Langhammer, C. Shrinking-hole colloidal lithography: Self-aligned nanofabrication of complex plasmonic nanoantennas. *Nano Lett.* **14,** 2655–2663 (2014).

161. Gross, J. H. *Mass Spectrometry*. (Springer Berlin Heidelberg, 2011). doi:10.1007/978-3-642-10711-5

162. Goldstein, J. I. *et al. Scanning Electron Microscopy and X-ray Microanalysis*. (Springer US, 2003). doi:10.1007/978-1-4615-0215-9

163. Williams, D. B. & Carter, C. B. *Transmission electron microscopy: A textbook for materials science*. (Springer US, 2009). doi:10.1007/978-0-387-76501-3

164. Mao, P. & Han, J. Fabrication and characterization of 20 nm planar nanofluidic channels by glass–glass and glass–silicon bonding. *Lab Chip* **5,** 837 (2005).

165. Ida, N. *Sensors, Actuators, and their Interfaces: A Multidisciplinary Introduction*. (Institution of Engineering and Technology, 2013). doi:10.1049/SBCS502E

166. Siemens, C. W. The Bakerian Lecture: On the Increase of Electrical Resistance in Conductors with Rise of Temperature, and Its Application to the Measure of Ordinary and Furnace Temperatures; Also on a Simple Method of Measuring Electrical Resistances. *Proc. R. Soc. London* **19,** 443–445 (1870).

167. Van Dusen, M. V. Platinum-resistance thermometry at low temperatures. *J. Am. Chem. Soc.* **47,** 326–332 (1925).

168. Beskok, A. & Karniadakis, G. E. Report: A model for flows in channels, pipes, and ducts at micro and nano scales. *Microscale Thermophys. Eng.* **3,** 43–77 (1999).

169. Zhang, H. *et al.* Direct Assembly of Large Area Nanoparticle Arrays. *ACS Nano* **12,** 7529–7537 (2018).

170. Gargiulo, J., Cerrota, S., Cortés, E., Violi, I. L. & Stefani, F. D. Connecting Metallic Nanoparticles by Optical Printing. *Nano Lett.* **16,** 1224–1229 (2016).